1530

COLLÈGE DE FRANCE

PHOTOSENSITIVE GAS DETECTORS FOR THE RING-IMAGING CHERENKOV (RICH) TECHNIQUE AND THE DELPHI BARREL RICH PROTOTYPE

R. Arnold[3], P. Baillon[1], J.D. Berst[3], H.J. Besch[2], M. Bosteels[1], E. Christophel[3], Y. Giomataris[5], J.L. Guyonnet[3], G. Passardi[1], J. Séguinot[2], J. Tocqueville[2], D. Toet[4] and T. Ypsilantis[2].

invited talk given by J. Séguinot at the Vienna Conference on MW chambers - 25 - 28 february 1986.

LPC/86-09

Laboratoire de Physique Corpusculaire

11, Place Marcelin-Berthelot, 75231 Paris CEDEX 05

Téléphone: (1) 43 29 12 11

PHOTOSENSITIVE GAS DETECTORS FOR THE RING-IMAGING CHERENKOV (RICH) TECHNIQUE AND THE DELPHI BARREL RICH PROTOTYPE

R. Arnold[3], P. Baillon[1], J.D. Berst[3], H.J. Besch[2], M. Bosteels[1], E. Christophel[3], Y. Giomataris[5], J.L. Guyonnet[3], G. Passardi[1], J. Séguinot[2], J. Tocqueville[2], D. Toet[4] and T. Ypsilantis[2].

invited talk given by J. Séguinot at the Vienna Conference on MW chambers - 25 - 28 february 1986.

LPC/86-09

1) CERN, Geneva, Switzerland.

2) Collège de France, Paris, France.

3) Centre de Recherches Nucléaires et Université Louis Pasteur, Strasbourg, France.

4) NIKHEF, Amsterdam, The Netherlands.

5) National Technical University, Athens, Greece. Now at CERN, Geneva, Switzerland.

ABSTRACT

After a short introduction to the ring-imaging technique, the principal types of photosensitive gas detectors are discussed. In the second part, status and results of the DELPHI barrel RICH prototype are presented. A short description of a possible very fast RICH for future hadron colliders is given.

RESUME

Après une courte introduction sur la technique de formation image de la radiation Cherenkov, les principaux types de détecteurs photosensibles sont discutés. Dans la seconde partie, le présent statut et les résultats du BARREL RICH DELPHI, sont présentés. Une courte description de la possible réalisation d'un détecteur RICH très rapide pour les futurs collisionneurs hadroniques est donnée.

1. INTRODUCTION

The Ring-Imaging Cherenkov (RICH) technique has been developed over the past 10 years for charged-particle—mainly hadron—identification. It covers a wide range of momenta over a large solid angle and provides simultaneous identification of several particle types even at high spatial and angular particle densities. The technique uses photosensitive gas detectors with moderate resolution and high granularity to determine the Cherenkov angle of ultraviolet (UV) photons emitted in a transparent radiating medium. Figure 1 shows how rings of photoelectrons are obtained by focusing the photons emitted in a gaseous radiator with a parabolic (or spherical) mirror and by propagating the photons emitted in a thin (5 to 10 mm) liquid radiator over a 10 to 20 times larger distance into the photosensitive volume. The latter method is called proximity focusing. Solid radiators cannot be used because their Cherenkov angle is larger than the total internal reflection angle. The resolution $\Delta\gamma/\gamma$ is given by

$$\Delta\gamma/\gamma = \gamma^2\beta^3 \, n \, \Delta\theta_c/\sqrt{(N_0 L)}$$

(γ = Lorentz factor E/m, β = v/c, n = index of refraction, L = radiator length). $\Delta\theta_c$ is the resolution in Cherenkov angle for one photon. N_0 is a quality factor related to the Frank and Tamm formula, which gives the number of radiated photons per length and photon energy interval as

$$dN/dEdL = (\alpha/\hbar c) \sin^2 \theta_c$$

(α = fine structure constant, $\hbar$ = Planck's constant, c = velocity of light, E = photon energy). Then the number of photoelectrons detected is

$$N_{pe} = L \sin^2 \theta_c \, N_0$$

$$N_0 = \alpha/\hbar c \int Q_{eff}(E) \prod_i \epsilon_i (E) \, dE.$$

(Q_{eff} = Quantum efficiency of the photodetector; ϵ_i are the efficiencies concerned, such as transmissions of boundaries, mirror reflectivity, absorption effects, etc.). So, for fixed n, $\Delta\gamma/\gamma$ is inversely proportional to the square root of the number of photons detected and directly proportional to the single-photon Cherenkov angle error. This error is mainly determined by the spatial resolution of the photon detector, the chromatic aberrations, and the imaging errors caused by the mirror or the radiator thickness in the case of proximity focusing. Triethylamine (TEA) with a threshold of 7.4 eV [1] and tetrakis(dimethylamine)ethylene (TMAE) with a threshold of 5.4 eV [2] have already been used as photosensitive gases in experiments [3]. Figure 2 shows in detail the choice one has for radiators, windows, and the appropriate photosensitive compound. The SLD [4] at the SLAC Linear Collider and DELPHI [5] at LEP will have powerful particle identification with ring-imaging detectors over $\sim 4\pi$ solid angle, using TMAE and quartz windows with a combination of liquid (C_6F_{14}) and gas (C_5F_{12}) radiators.

2. PHOTON DETECTORS

A photon detector is, for our purposes, a photosensitive volume, or conversion gap, combined with a multiwire detector sensitive to one single photoelectron. The detector has to provide two- or three-dimensional information on the position of the photoelectron. Its resolution, and if possible granularity, has to match the errors in $\Delta\theta$ and its rate capability the experimental requirements. Present detectors fall into two distinct classes, 'fast' detectors with a time dispersion of less than a microsecond and 'slow' detectors which can have drift times of up to 30 μs.

2.1 'Fast' ring-imaging detectors

These detectors use a direct coupling between the conversion gap and a photoelectron detector, which is either a multiwire proportional chamber (MWPC) or a multistep avalanche chamber (MSAC) (fig. 3). The projected image in the detector plane is obtained by wire and cathode-strip readout. The time dispersion t_D is determined by the photon mean free path λ in the conversion gap and the electron drift velocity v_D. Consequently, $t_D \gtrsim 3\lambda/v_D$ for full absorption. If the parallax error becomes dominant for $\Delta\theta_c$ one needs drift-time measurement to obtain the conversion depth. A very fast RICH detector (t_D = 40–100 ns) needs a photon absorption length of 1 or 2 mm. Triethylamine is a good candidate for such detectors but, barring cryogenic liquids, can only be used with noble gases. This moves the threshold Lorentz factor γ_T to ~ 20 or more (cf. fig. 2). With TMAE one would need temperatures above 70°C for such a short photon absorption length. Small time dispersion may be necessary for future multi-TEV hadron machines. The high temperature is acceptable since particle identification at low γ_T is likely to be of little interest and no liquid radiators will be needed. A possible layout for a very fast RICH detector will be discussed later.

2.1.1 Multistep avalanche chambers (MSAC)

This technique is already well known and documented [6] and has been used in a Fermilab experiment [7]. Figure 4 shows the basic principle: photons entering through the window are converted in the conversion gap C; the electrons are then drifted into preamplifier gap PA with parallel-plate geometry. The transfer efficiency is good because the field in PA is much larger than in C. Part of the avalanche is then transferred into the transfer gap T and drifted into the wire chamber for second amplification and detection. The depths of C and T have both to be several photon absorption lengths.

These detectors have achieved very high gain, $> 10^6$ at atmospheric pressure and up to 10^8 at low pressure [8]. This is at least one order of magnitude higher than the gain achieved without preamplification, and is due to the fact that photons emitted in the high current avalanche in the wire chamber cannot feed back into the conversion volume C from where the overall gain is high, and thus cause afterpulses and eventually instability. Instead, they are absorbed in T, from where the overall gain is only a little more than the square root of the total gain. The photons generated in the small avalanches in PA are not copious enough to cause problems.

2.1.2 Resolution, timing properties, and multihit capability of a MSAC

The time dispersion of these systems is still $t_D \approx 3\lambda/v_D$ because the drift-time in T is a pure storage time which does not affect the counting-rate capability. The detector developed by

Charpak and Sauli [7] used TEA and conversion- and transfer-gap depths of 6 and 10 mm, respectively. The associated wire chamber had 1.3 mm wire distance and 5 mm wide cathode strips at $\pm 45°$ to the wire. (At least one cathode plane has to be made from wires.) This resulted in 40 ns time resolution and a submillimetre precision from the centroid method for the cathode strips. The two-photon resolution was 8 to 10 mm and the total number of photons was limited to 5 because of ambiguities.

Increasing the mean free path of the photon, e.g. by using TMAE, makes the time dispersion correspondingly worse and the acceptable number of photons per event correspondingly better by spreading them in time. This has been done in ref. [9] (fig. 4). The conversion and transfer gaps were 50 mm deep, the gas mixture was He (90%) + isobutane (10%) + TMAE at room temperature ($\sim 5 \times 10^{-4}$). The (saturated) drift velocity was 2 cm·μs^{-1}, resulting in a time dispersion of 2.5 μs. Using wave-form digitizers and correlating cathode and anode information, about 5 photoelectrons can be handled every 50 ns. Owing to the exponential distribution of arrival times about 120 photoelectrons can be accepted per event.

At low pressure, using a delay-line cathode readout, Breskin and Chechik [8] have achieved $\sim$ 1 mm spatial resolution. Low-pressure detectors have the additional advantage of being insensitive to fast particles crossing the conversion gap.

2.2 'Slow' RICH detectors

This class of detector (fig. 5) was developed by the RICH group (Caen–CERN–Collège de France–Ecole Polytechnique) [10] and proposed in 1981 for a large-acceptance detector at moderate cost. Photoelectrons created in the conversion volume are drifted in a homogeneous electric field towards a multiwire detector at one end. This detector can be either a MSAC or a MWPC. The latter is commonly used. The wire address and associated drift-time gives an ambiguity-free two-dimensional image, allowing the separation of overlapping rings from a multiparticle event. The parallax error for inclined photons can be corrected by measuring the depth of the conversion with a cathode-strip readout or a charge-division method. This gives rise to ambiguity problems for synchronously arriving photoelectrons.

2.2.1 MWPC detectors

It has been demonstrated that single-stage MWPCs are fully efficient for single-photon counting, using CH_4, C_2H_6, iso-C_4H_{10}, or any mixture of them as the carrier gas for the photosensitive compound. Isobutane is better avoided though, because it is slightly electronegative and not transparent below 168 nm. With a maximum gain of 1 to 2×10^5 a threshold of 30 to 50 nA has to be used. The gain is limited by UV photons from the avalanche feeding back into the conversion volume and generating secondary avalanches. At a mean gain of 2×10^5 and a TMAE temperature of 27°C, the measured probability of observing a feedback avalanche is 10% per incoming electron. This means that a charged particle crossing a 5 cm deep conversion gap and generating 300 to 500 electrons through ionization can completely obscure its own Cherenkov ring or at least degrade the resolution. The photon feedback has to be suppressed by at least an order of magnitude to make a single-step MWPC operational. Several types of feedback-suppressing chambers have been developed for DELPHI and SLD.

2.2.2 The 'cloison' chamber

This type of chamber (fig. 6)—the first safe single-stage single-photon detector [11]—uses 'cloisons' (blinds) between sense wires to decrease the wire-to-wire coupling and to suppress the solid angle for feedback photons by a factor of 10. The cloisons are made of Kapton (200 μm) and carry several potential strips on each side to control the gain and to shape the field towards the 20 μm anodes, assuring high transfer efficiency and good isochronism. A stable gain of 5×10^5 was achieved at operating voltages of 1600 to 1700 V depending on the gas mixture. Later developments of these chambers used alumina cloisons and were equipped with cathode-strip (4 mm wide) readout. To get an even moderate cathode signal of about 30% of the anode signal, the anode wire has to be very close to the cathode (0.5–0.8 mm). This requires a high mechanical precision to achieve a homogeneous gain. If the chamber has to be gated for space-charge reasons, one or two additional wire planes are required in front of the cloisons. So this type of chamber becomes quite intricate to build. It has the advantage, though, of remaining fully efficient in magnetic fields of 1.3 T orthogonal to the wire plane, and, with ethane as carrier gas, even in magnetic fields of the same strength parallel to the wires, in spite of a Lorentz angle of about 50° [12, 13]. The original idea of the cloison chambers was born in the RICH group and further developed at Amsterdam, Cracow, Strasbourg, and Uppsala.

2.2.3 'Minitube' detectors

This type of detector [14] is a MWPC with a cylindrical cathode (fig. 7). It is made of stainless-steel tubes 60 mm long with 2 mm inner and 2.5 mm outer diameter. The tubes are mounted side by side and cut open parallel to their axis at the side facing the drift volume. The shaped slit is 0.8 mm wide and the anode wire, centred in the tube, has 20 μm diameter. The assembled tubes are cut every 5 mm at right angles to the anode wire to form cathode strips. The large solid angle of the cathode strips—which nearly surround the sense wires—assures a maximum induced charge on the strips. For low-impedance preamplifiers this gives a resolution of $5/\sqrt{12} \approx 1.5$ mm (or better) even without charge measurement on the cathodes. In reality, the resolution is somewhat worse owing to signal diffusion due to strip-to-strip capacitance and finite input impedance of the preamplifiers. Chambers of this type, developed at the Collège de France and the CRN Strasbourg, had a strip-to-strip capacitance of 9 pF (for 36 tubes) which gave, with a 650 Ω input impedance, an average of 1.9 cathode hits per single-electron anode hit.

Two planes F_1 and F_2 of 50 μm field-shaping wires, 8 mm above the sense wires and arranged as in fig. 7, focus the photoelectrons through the slit. These wire planes also provide the possibility of an efficient gating of the chamber to prevent the positive ions of the avalanches from going backwards into the drift volume. Gating voltages of ± 100 V are sufficient (without magnetic field) to reduce the positive-ion current by more than 3 orders of magnitude. Positive ions are, as discussed later, the most important source of image distortions in the drift volumes. The central wire F_2 picks up about 10% of the electric flux, thus leading to a maximum transfer efficiency of about 90%. In practice these chambers were found to be no less efficient than cloison chambers. In a magnetic field of 1.2 T normal to the wire plane incoming photoelectrons are displaced along the wire by less than 0.5 mm ($E \times B$ effect) and the focusing is weakened, leading to a reduction of the transfer efficiency. This loss has been measured to be 26% for pure methane. It will be smaller for methane–ethane mixtures and can, as calculations have shown, be avoided completely with a third focusing plane [12].

Cloison and minitube chambers, the first without the latter with cathode readout, have been used for at least one year on the prototype of the DELPHI barrel RICH. After initial burn-in both types of chambers showed very good operational reliability.

2.2.4 Charge-division detectors

For the SLD Cherenkov Ring Imaging Detector (CRID), chambers are under development which use low metallic blinds and additional shielding and focusing wires. The sense wires are 7 μm diameter carbon fibres, which have a sufficiently high resistivity ($\varrho = 1600\ \mu\Omega \cdot$ cm) to allow a determination of the coordinate along the wire by charge division. For a 5 cm long wire operated at an average gain of 2×10^5 the error in the longitudinal position was measured to be $\sigma_L/L = 2\%$ ($\simeq$ 1 mm). This is a good result (fig. 8). The technique is certainly more expensive and electronically more complicated and—because of the necessary charge calibrations—more difficult to use than the cathode-readout method, but it has the important advantage of avoiding the problem of achieving a good cathode efficiency.

2.2.5 An illustration of the long-drift technique: the DELPHI barrel RICH

This detector (fig. 9) has been designed for π, K, and p separation between 0.3 and 25 GeV/c. It is of annular shape and has an inner radius of 1.28 m, an outer radius of 1.97 m, and an active length of about 3 m, and surrounds a time projection chamber (TPC) tracking detector [5]. The detector combines liquid and gas radiators located on the opposite sides of a single photosensitive drift volume, 5 cm thick and 2×1.6 m long, to cover a polar angle of $2 \times 42°$ relative to the central plane. In azimuth the same configuration is repeated every 10° or 15° to fit into a circular shape.

The liquid radiator is a 1 cm thick layer of perfluorohexane C_6F_{14} at a distance of 12 cm from the drift volume and operates in the proximity-focusing mode. The index of refraction of this radiator is 1.278 and consequently its threshold $\gamma_T = 1.6$. The gas radiator consists of perfluoropentane C_5F_{12} at atmospheric pressure, $\gamma_T = 16.8$, and its Cherenkov light is focused with parabolic mirrors of about 45 cm focal length into the photosensitive drift volume.

The total photosensitive area is about 27 m^2; the axial electric field is 0.6 kV$\cdot$cm^{-1} embedded in a magnetic field of 1.2 T which is also axial. With a gas mixture of CH_4 (75%) + C_2H_6 (25%) + TMAE the maximum drift-time is $\sim$ 25 μs. The detector operates at a temperature of 310 K. The TMAE partial pressure is set by its vapour pressure at 300 K. Drift-times are measured with 12 bit time-to-digital converters (TDCs) with an 8 ns time bin.

2.2.6 Limitations of the long-drift technique

Assuming the electric field is uniform in the drift volume, and no space and surface charges are present, then the spatial reconstruction error for the photoelectrons is dominated by electron diffusion in the drift volume: keeping the geometry of the DELPHI barrel RICH in mind, and using an obvious system of cylinder coordinates, one finds

$$\langle\sigma_R\rangle = [(w^2/12) + (4/9)\,\sigma_T^2 L]^{1/2} = [(1.44\text{ mm})^2 + (1.43\text{ mm})^2]^{1/2} \approx 2\text{ mm}$$
$$\langle\sigma_{R\phi}\rangle = [(s^2/12) + (4/9)\,\sigma_T^2 L]^{1/2} = [(0.73\text{ mm})^2 + (1.43\text{ mm})^2]^{1/2} \approx 1.6\text{ mm}$$
$$\langle\sigma_z\rangle = [(\delta t)^2\, v_D^2 + (4/9)\,\sigma_L^2 L]^{1/2} = [(0.6\text{ mm})^2 + (1.43\text{ mm})^2]^{1/2} \approx 1.6\text{ mm}\,.$$

(Wire spacing s = 2.54 mm, cathode strip width w = 5 mm, drift length L = 1.6 m, diffusion coefficient $\sigma_L = \sigma_T = 170\ \mu m \cdot cm^{-1/2}$, v_D = drift velocity = $6.73\ cm \cdot \mu s^{-1}$. The time resolution δt is a combined effect of preamplifier slewing, discriminator slewing, and TDC time binning: $\delta t \approx 10$ ns.)

However, if one compares the other errors which contribute to the Cherenkov-angle determination, one observes (fig. 10):

i) for the liquid radiator a good match between the reconstruction error in space and the combined contribution of the chromatic aberration and the geometric error due to radiator thickness;

ii) for the gas radiator, owing to the short focal length used, a clear dominance of the reconstruction error, which should be improved if possible.

The long-drift technique is fairly cheap: for a 1 m^2 active photosensitive surface one needs about 400 electronic channels, giving about 3.5×10^7 pixels in the corresponding volume.

3. THE BARREL RICH PROTOTYPE

A full-scale prototype of the DELPHI barrel RICH was built in 1983 to study the feasibility and the performances of a big RICH system.

The prototype has the same configuration as the final detector; it has full length and covers a 25° sector in azimuth (figs. 11, 12). It consists of 3 photosensitive drift tubes, 170 cm long with 18×5.2 cm^2 inner mean cross-section; and 15 cm below there is a single liquid radiator of the same length, filled with C_6F_{14}. Above the central drift volume is a gas radiator and a row of 1 parabolic and 3 spherical mirrors. Isobutane ($\gamma_T = 18$) and C_5F_{12} ($\gamma_T = 16.8$) have been used as radiators at atmospheric pressure. These components are housed in a cylindrical container of 90 cm inner diameter and 2.5 m length.

3.1 The field-shaping system

The liquid-radiator box and the drift tubes are built with a hybrid technique. They are made of glass-fibre-reinforced expoxy where they can be non-transparent and quartz plates where they have to be transparent. All surfaces have their potential defined every 2.54 mm along the drift direction z. This is done with printed-circuit Kapton foils carrying strips and glued onto the epoxy parts or with 100 μm CuBe wires wrapped around the quartz plates. In addition, there is a coarse wire plane 10 cm above the drift boxes. To avoid a perturbation, the container itself is made from 30 layers of 50 μm copper sheets, separated by 0.8 mm of glass-reinforced expoxy cured under vacuum. These copper sheets increase in length and azimuth from the innermost to the outermost layer carrying the potential gradually (and linearly) from the central high-voltage plane to ground. The inside of the container is covered with a Kapton printed circuit, carrying strips again every 2.54 mm. All strips and copper sheets at the same voltage are joined together with simple connectors and are supplied from one single divider chain to ensure a good homogeneity of the drift field. High voltages, up to 100 kV, corresponding to an electric field of $600\ V \cdot cm^{-1}$, were used. Most of the tests were done with the maximum voltage and a divider chain current of 0.6 mA. The whole of the detector is thermally isolated and heated to about 35°C.

The quality of the electric field was tested with a $10\ GeV \cdot c^{-1}$ pion beam passed through the drift boxes. The mean drift time τ, averaged over all wires of the detector, and the variance from

a straight-line fit, σ^2, increase linearly with the drift distance z (fig. 13). From the data one can derive that longitudinal field inhomogeneities in the drift volume are less than 3‰ and that the diffusion coefficient for the CH_4–iso-C_4H_{10} mixture used is 170 $\mu m \cdot cm^{-1/2}$, well in agreement with published data. To avoid losses by diffusion and field inhomogeneities the drift tubes are slightly conical in one dimension.

3.2 Imaging errors in the drift tubes

Severe transverse imaging errors, of up to 2 cm, were found in the drift tubes: drifting electrons were pushed towards the centre of the tube. This distortion was caused by positive ions in the drift tube. It was studied with a set of UV flash lamps (fig. 14) illuminating the drift volume through equally-spaced small holes in a mask at 3 different drift distances. The flash frequency of 5 per second was low enough to collect all positive ions between two successive flashes. A space charge of up to 1.5×10^7 ions per cubic centimetre could be generated with an additional flash lamp running randomly at high frequency.

Figure 15a shows, as an example, for 1 m drift distance the deviation $x_{meas} - x_{th}$ between the observed and the expected position of the light spots. It is visible that the deviations near the side walls are really large ($\sim$ 20 mm) for a space charge of 1.5×10^7 ions per cubic centimetre, a figure quite representative for test-beam conditions. The distortions can be drastically reduced either by turning off the space charge or by gating the transfer into the MWPC. There remain, however, residual deviations which give rise to a systematic error if they are not used as a correction. A similar focalization exists in the orthogonal direction. It is more important in the central region of the tube around $x = 0$ than along the side walls. An x- and y-dependent shift of the drift-time is also observed.

Figure 15b shows the imaging errors of the tube for x and z as measured with the flash lamps during the spill at very low beam intensity. Consequently, an accurate reconstruction in space needs a three-dimensional correction, which for most of the tube's volume is less than 1.5 mm (gating implied) but in a few places can increase to 6 mm.

3.3 Ring-imaging beam tests

The most important ingredients for good Cherenkov ring images are clean gases and liquids and permanent monitoring of their properties. All gases were purified in one or two stages of an Oxisorb system and the liquid radiator was cleaned by closed circulation through an Oxisorb cartridge. Insufficient cleaning easily resulted in a loss of 70% of the photoelectrons. The UV photon mean free path in the radiators and the conversion (drift) volume was monitored with a monochromator. The oxygen content in the carrier gas for the TMAE was measured with a commercial oxygen meter and kept below 1 ppm. Typical radiator transparencies are shown in fig. 16, together with the quartz transparencies and the TMAE quantum efficiency. These measured values have been used as input for the Monte Carlo simulations.

3.3.1 Effects of the beam on the detector

For the tests described in the remaining part of this report the prototype was equipped with three minitube detectors. For part of the tests one of the mirrors was mounted with its axis normal to the drift tube (cf. fig. 12). Superimposed ring images obtained in this configuration from 50 pions of 10 GeV/c are shown in fig. 17. One can see the spot where the beam crosses the

drift volume (parallel to the sense wires) and the rings from the liquid and gaseous radiators. The photon mean free path in the $CH_4 + C_2H_6 +$ TMAE mixture was about 4 cm ($T_{TMAE} = 15°C$) and the drift distance was on the average 50 cm. The total number of hits per event is 40, of which 27 are due to photoelectrons in the rings. Figure 18 is an exploded view of the beam region showing the afterpulses due to reabsorbed photons generated by the large avalanches of the ionization track of the beam particles. These large avalanches also cause a long dead-time in the preamplifier, resulting in the empty region behind the beam. The drift-time spectrum of the afterpulses is also shown in fig. 18. Its exponential distribution has a photon mean free path which agrees very well with the mean free path measured in the monochromator. The total number of secondary photoelectrons is about 3.5 to 4 per event.

3.3.2 Improvement of the resolution by cathode readout

In fig. 19a one can see raw rings from the liquid radiator taken under similar conditions as before, at 47 cm drift distance and at a TMAE temperature of 25°C (15 mm photon absorption length). The discontinuity in the rings is due to the dead space between the drift tubes. In fig. 19b—using the information of the cathode readout—the photoelectrons of the rings are projected along the Cherenkov cone into the central plane of the drift tube. One can clearly see how the sharpness of the rings improves. This is quantitatively demonstrated in fig. 20a. The standard deviation of the Cherenkov angle of a photon improves from 28 to 12 mrad, when using the cathode-strip information. For the gas images taken at normal incidence the improvement is much less important as a consequence of the small opening angle of the Cherenkov cone (fig. 20b). The resolution improves from 5.5 to 4.3 mrad. In these figures the error coming from the beam definition by hodoscopes is included. It is 3 mrad for the liquid and 2.2 mrad for the gaseous radiator. Corrections for space-charge effects have not been applied.

When one compares, in fig. 20c, the Cherenkov angle distribution for the liquid radiator with its Monte Carlo simulation, without using the strip information, one finds a good agreement. This proves that the difference observed if one includes the strip information is mainly due to space- and surface-charge effects, dominating the reconstruction error in depth.

3.3.3 Images at oblique angles of incidence of the beam

If one turns away the angle of incidence from the normal to the drift tube, the rings from the liquid radiator take on first an elliptic, and later a hyperbolic, appearance. (They are not exactly conic sections owing to refraction at the surface of the liquid radiator.) At the same time, additional background sources appear because Cherenkov light generated in the quartz windows can escape. Figure 21 shows an example of such an image together with its Monte Carlo counterpart, taken at 21.7° from the normal. The number of photoelectrons in the ring has already decreased by a factor of 2 because about one half of the cone is lost by total internal reflection.

3.3.4 Photoelectron absorption in the drift tubes

Rings from the liquid radiator have also been used to determine the absorption length of the photoelectrons in the drift tube by measuring their number as a function of the drift distance. Because uncorrelated background has a flat distribution in a $(1/R)(dN_{pe}/dR)$ plot (fig. 22a) these plots have been used for background subtraction.

The result is shown in fig. 22b. There is barely any absorption visible and the absorption length is more than 10 m. This value was consistently achieved or surpassed after the oxygen had been removed from the drift gas, isobutane was no longer used in the drift tubes, the gas flow was modified from longitudinal to transverse to avoid stratification, and finally the TMAE had been properly cleaned by washing it with water.

3.4 Resolution: experimental results and Monte Carlo calculation

The resolution of the single-photon Cherenkov angle for the liquid radiator is shown in fig. 23 as a function of distance at normal beam incidence. There is a significant difference between data and Monte Carlo calculation. As already explained, it is caused by vertical (along y) focalization due to space charge and surface effects. At the time of data taking, the cathode readout and the gating of the detectors could not yet be used simultaneously to diminish this effect. The same remarks apply to fig. 24, where the angle of incidence has been varied with the drift distance to follow the orientation of the mirrors. Because of the oblique incidence the discrepancies between data and simulation for the gas radiator are somewhat larger than in fig. 20b.

The results on the overall efficiency are summarized in table 1. Over one year they have been repeatedly and consistently achieved as long as the gases and liquids were properly cleaned. The merit factor $N_0 = 57\ cm^{-1}$ for the liquid-radiator rings is not corrected for the losses between drift tubes. With this correction the effective value is $65\ cm^{-1}$. The values of $69\ cm^{-1}$ and $80\ cm^{-1}$ for the isobutane and C_5F_{12} gaseous radiators are exactly what we expect from our knowledge of the TMAE quantum efficiency, the transparencies, and the mirror reflectivity. By better purification of the C_5F_{12}, N_0 can be better than $90\ cm^{-1}$.

With the exception of the liquid-radiator resolution—and in this case it is obvious what to do—all expected performances given in the DELPHI proposal [5] have been met or surpassed.

The results of the prototype have shown that the RICH technique with photosensitive gases is now well developed for application in large detectors and has made tremendous progress since it was first proposed [17]. One has to watch out, however, not to lose most of the performance by an accumulation of small mistakes.

4. OUTLOOK: FAST RICH DETECTORS FOR HADRON COLLIDERS

Future pp colliders will have short bunch distances of a few tens of nanoseconds and interaction rates of up to $10^8\ s^{-1}$. While one can tolerate some overlap of events—most of them are of the uninteresting minimum-bias type—one would prefer a fast collection of the information. In the following some ideas are presented as to how one could build a RICH detector with about 30 ns collection time.

Particle identification at low momenta is probably not very important, so one should concentrate on focusing counters with gaseous radiators, and extend the identification range to about 100 GeV/c. This requires radiator and focal lengths of about 1 m, permitting a good match of detector resolution and chromatic error.

A simple photon detector using TMAE is shown in fig. 25. It is a MWPC with $CH_4 + C_2H_6$ as the carrier gas, working above 70°C to keep the photon mean free path below 1.5 mm.

The wire spacing is 2 mm, and the cathode plane is divided into pads of $4 \times 4\ mm^2$ to obtain good multiphoton capability. The single-photon resolution Δ_{θ_c} will be 1.2 mrad for a focal length

of 1 m. The anode 'wires', of 20 μm diameter, are made of metallized quartz fibres to minimize differential thermal expansion and to allow a segmentation of the conductive part in stretches of 5 cm. The distance between the cathode planes is about 3 mm to absorb at least 90% of the photons. The distance between anode and cathode pads has to be decreased as much as possible below 1 mm to optimize the induced signal on the cathode. Owing to the small thickness of the gas layer the ionization of charged particles crossing the detector should not cause problems and, in view of the very short photon mean free path, one can probably avoid 'cloisons' between wires. A true cylindrical geometry can easily be used. The cost is mainly determined by the large number of miniaturized preamplifiers needed ($\sim 7 \times 10^4 \cdot m^{-2}$) and is likely to be 3 to 5 times higher than for a slow RICH detector.

Acknowledgements

U. Amaldi has strongly encouraged and supported us in the prototype work. We have had a lot of competent help. For this we would like to thank C. David, J. Dixon, D. Fraissard, P. Frandsen, G. Geydet, J.P. Huber, W. Klempt, Y. Kornelis, L. Lanceri, G. Mourgue, J. Perez, P. Queru, P. Rada, J. Raynaud, E. Rosso, A. Therond and J. Tischhauser, from CERN; J.P. Jobez and R. Saigne, from Collège de France; N. Amrane, E. Aria, T. Calligaro, M. Dracos, R. Fischer, N. Mayet, R. Oswald, J. Persigny and R. Priss, from CRN Strasbourg; and N. de Koning and T. Ypma, from NIKHEF. The University of Oslo has contributed to the positioning system of the prototype. The Ecole Polytechnique (Paris) has provided part of the data-acquisition system. The CERN PS Operations Group, and especially K. Bätzner, have developed for us special low-background beam conditions. We want to thank them for these very important contributions. We would also like to thank M. Crozon, M. Froissart and M. Schaeffer for the interest they have taken in our work. We are grateful to P. Pétroff, from LAL, Orsay, who has examined the behaviour of cloison and minitube chambers in a magnetic field.

Finally we acknowledge most sincerely the support of those who have paid for everything: the European taxpayers.

REFERENCES

[1] G. Charpak and F. Sauli, Phys. Lett. **78B** (1978) 523.
G. Charpak, S. Majewski, G. Melchart, F. Sauli and T. Ypsilantis, Nucl. Instrum. Methods **164** (1979) 419.
J. Séguinot, J. Tocqueville and T. Ypsilantis, Nucl. Instrum. Methods **173** (1980) 283.
T. Ekelöf, J. Séguinot, J. Tocqueville and T. Ypsilantis, Phys. Scr. **23** (1981) 718.

[2] D.F. Anderson, IEEE Trans. Nucl. Sci. **NS-28** (1981) 842.
E. Barrelet, T. Ekelöf, B. Lund-Jensen, J. Séguinot, J. Tocqueville, M. Urban and T. Ypsilantis, Nucl. Instrum. Methods **200** (1982) 219.
E. Barrelet, T. Ekelöf, B. Lund-Jensen, J. Séguinot, J. Tocqueville, M. Urban and T. Ypsilantis, Proc. Int. Conf. on High-Energy Physics, Lisbon, 1981 (EPS, 1982), p. 1066.

[3] R.J. Apsimon, P.S. Flower, K.A. Freeston, G.D. Hallewell, J.A.G. Morris, J.V. Morris, C.N. Paterson, P.H. Sharp, C.N. Uden, M. Davenport, J. Eades, P.A. Coyle, D. Mercer, S. Danaher, R.H. McClatchey, N. Thacker and L.F. Thompson, The recent operational performance of the CERN Omega Ring Imaging Cherenkov Detector, to be published in Proc. IEEE 1985 Nuclear Science Symposium, San Francisco.
M. Adams, A. Bastin, G. Coutrakon, H. Glass, D. Jaffe, J. Kirz, R. McCarthy, J.R. Hubbard, Ph. Mangeot, J. Mullie, A. Peisert, J. Tichit, R. Bouclier, G. Charpak, J.C. Santiard, F. Sauli, J. Crittenden, Y. Hsiung, D. Kaplan, C. Brown, S. Childress, D. Finley, A. Ito, A. Jonckheere, H. Jöstlein, L. Lederman, R. Orava, S. Smith, K. Sugano, K. Ueno, A. Maki, Y. Hemmi, K. Miyake, T. Nakamura, N. Sasao, Y. Sakai, R. Gray, J. Rothberg, J. Rutherfoord and K. Young, Nucl. Instrum. Methods **217** (1983) 237.

[4] SLD Design Report, SLAC-273 (1984).

[5] DELPHI Technical Proposal, CERN/LEPC/83-3 (1983).

[6] A. Breskin, G. Charpak, S. Majewski, G. Melchart, G. Petersen and F. Sauli, Nucl. Instrum. Methods **161** (1979) 19.
R. Bouclier, G. Charpak, A. Cattai, G. Million, A. Peisert, J.C. Santiard, F. Sauli, G. Coutrakon, J.R. Hubbard, Ph. Mangeot, J. Mullie, J. Tichit, H. Glass, J. Kirz and R. McCarthy, Nucl. Instrum. Methods **205** (1983) 403.

[7] H. Glass, M. Adams, A. Bastin, G. Coutrakon, D. Jaffe, J. Kirz, R. McCarthy, J.R. Hubbard, Ph. Mangeot, J. Mullie, A. Peisert, J. Tichit, R. Bouclier, G. Charpak, J.C. Santiard, F. Sauli, J. Crittenden, Y. Hsiung, D. Kaplan, C. Brown, S. Childress, D. Finley, A. Ito, A. Jonckheere, H. Jöstlein, L. Lederman, R. Orava, S. Smith, K. Sugano, K. Ueno, A. Maki, Y. Hemmi, K. Miyake, T. Nakamura, N. Sasao, Y. Sakai, R. Gray, R. Plaag, J. Rothberg, J. Rutherford and K. Young, IEEE Trans. Nucl. Sci. **NS-30** (1983) 30.

[8] A. Breskin, G. Charpak and S. Majewski, Nucl. Instrum. Methods **220** (1983) 349.
A. Breskin and R. Chechik, IEEE Trans. Nucl. Sci. **NS-32** (1985) 504.

[9] F. Sauli and G. Charpak, IEEE Trans. Nucl. Sci **NS-32** (1985) 663.

[10] E. Barrelet et al., see ref. [2].
E. Barrelet, J. Séguinot, M, Urban, T. Ypsilantis, T. Ekelöf, B. Lund-Jensen and J. Tocqueville, Proc. 1981 Isabelle Summer Workshop, Upton, NY (BNL 51443, 1981), Vol. 4, p. 1378.

[11] L.O. Eek, T. Ekelöf, K. Fransson, A. Hallgren, P. Kostarakis, G. Lenzen, B. Lund-Jensen, J. Séguinot, J. Tocqueville and T. Ypsilantis, IEEE Trans. Nucl. Sci. **NS-31** (1984) 949.

[12] P. Baillon, H.J. Besch, E. Christophel, J.L. Guyonnet, P. Pétroff, J. Séguinot, D. Toet and T. Ypsilantis, DELPHI 85–99, RICH 10 (1986) (Internal Report of the DELPHI Collaboration).

[13] A. Hallgren, private communication.
W. Dulinski, L.O. Eek, T. Ekelöf, K. Fransson, A. Hallgren, P. Kostarakis, G. Lenzen, P. Lorenz, B. Lund-Jensen, J. Michalowski and M. Turala, contribution to this conference.

[14] All available information is scattered around in various unpublished proceedings of the DELPHI Collaboration.

[15] F. Bird, S. Shapiro, V. Ashford, D. McShurley, R. Reif, D.W.G.S. Leith and S. Williams, to be published in Proc. IEEE 1985 Nuclear Science Symposium, San Francisco.

[16] DELPHI Progress Report, CERN/LEPC 84–16 (1984).

[17] J. Séguinot and T. Ypsilantis, Nucl. Instrum. Methods **142** (1977) 377.

Table 1

Overall efficiency of the DELPHI barrel RICH prototype

	Radiator		
	Liquid L = 1 cm C_6F_{14}	Gas L = 47 cm iso-C_4H_{10}	Gas L = 47 cm C_5F_{12}
N_{pe} [a)]	21.5	10	13
$\langle n - 1 \rangle$ measured		15.4×10^{-4}	17.2×10^{-4}
N_0 (cm^{-1})	57	69	80
N_0 corrected for dead space	65		

a) N_{pe} is the number of photoelectrons in the Cherenkov ring.

Figure captions

Fig. 1 a) Principle of Cherenkov Ring Imaging.
b) Typical rings from liquid and gaseous radiators.

Fig. 2 Range of transparency and γ_T for different radiating media together with TMAE and TEA quantum efficiencies and window transmissions.

Fig. 3 Principle of a fast RICH detector.

Fig. 4 Principle of a multistep avalanche photon detector.

Fig. 5 Principle of a slow RICH detector using electron drift over long distances.

Fig. 6 'Cloison' chamber.

Fig. 7 'Minitube' detector.

Fig. 8 Results from the SLD photodetector using charge-division readout.
a) Linearity of the charge asymmetry $A_Q = (Q_L - Q_R)/(Q_L + Q_R)$.
b) Total charge Q_T plotted against asymmetry A_Q.
c) Asymmetry A_Q.
b) and c) are taken at the centre of the wire.

Fig. 9 Longitudinal cut of a tentative design of the DELPHI barrel RICH.

Fig. 10 Single-photon mean errors at normal incidence for liquid and gas radiators as a function of the Lorentz factor γ at 1 m drift distance.

Fig. 11 Artist's view of the DELPHI barrel RICH prototype.

Fig. 12 Longitudinal cut of the DELPHI barrel RICH prototype.

Fig. 13 Variation of drift time τ and diffusion σ^2 with drift distance.

Fig. 14 Ultraviolet flash-lamp set-up for the study of imaging errors.

Fig. 15 a) Deviation $\Delta x = x_{meas} - x_{th}$ for different space-charge and gating conditions.
b) Δx and Δz at very low beam intensity (100 π^-/s).

Fig. 16 Typical measured transmission of windows and radiators.

Fig. 17 Superimposed rings from liquid and gas radiators at a drift distance of 46 cm and a TMAE temperature of 15°C.

Fig. 18 Expanded view of the beam region of fig. 17, and time distribution of reabsorbed photons.

Fig. 19 Superimposed rings from the liquid radiator reconstructed a) without and b) with strip information at a TMAE temperature of 25°C.

Fig. 20 Single-photon Cherenkov angle distributions with and without strip information: a) from the liquid, b) from the gas radiator. Comparison of data from the liquid radiator with a Monte Carlo simulation: c) without, d) with use of the strip information.

Fig. 21 Superimposed rings at an angle of incidence of 21.4° from the normal: a) raw data, b) Monte Carlo simulation.

Fig. 22 a) Weighted radius distribution of photoelectrons from the liquid radiator relative to the centre of the beam.
b) Variation of the number of detected photoelectrons with drift distance.

Fig. 23 Cherenkov-angle resolution for photons from the liquid radiator at normal beam incidence: experimental results and Monte Carlo calculation (suppressed zero!).

Fig. 24 Cherenkov-angle resolution at oblique incidence of the beam.

Fig. 25 Tentative design for a very fast RICH detector.

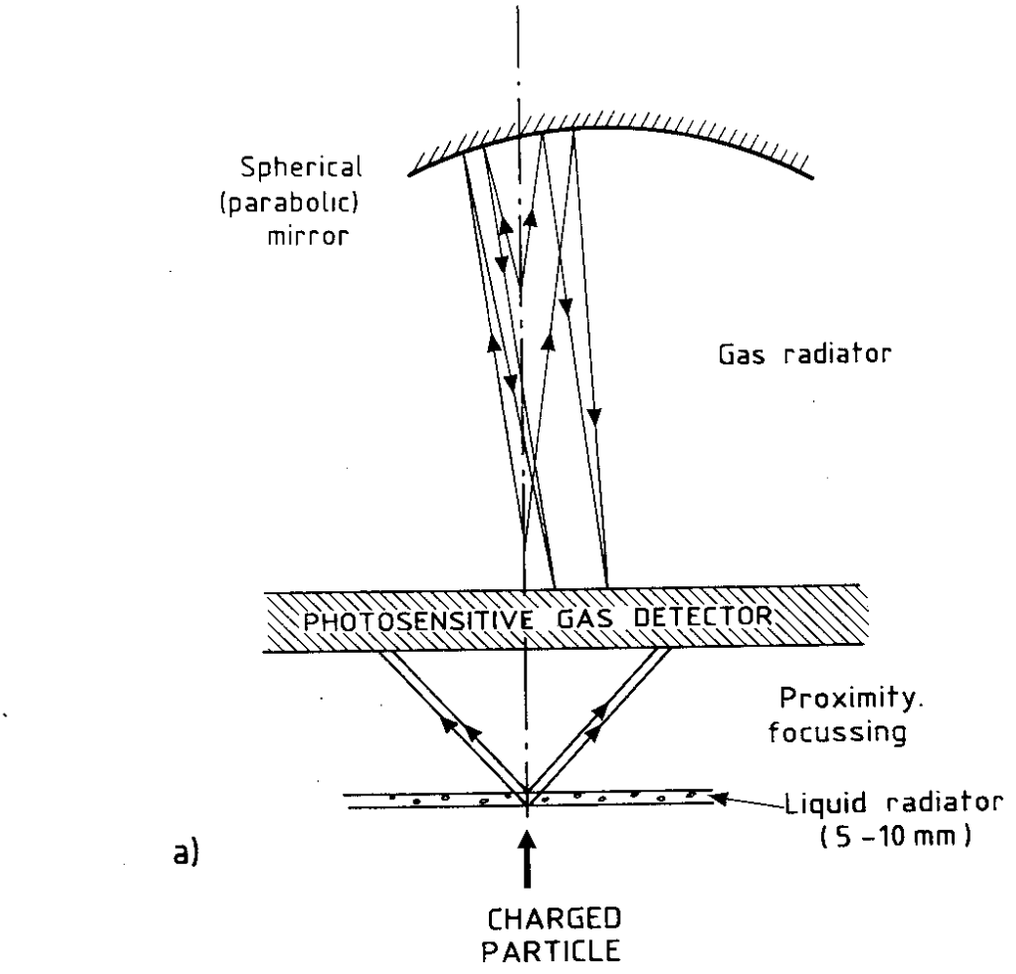
Spherical
(parabolic)
mirror
Gas radiator
PHOTOSENSITIVE GAS DETECTOR
Proximity.
focussing
Liquid radiator
(5 -10 mm)
a)
CHARGED
PARTICLE

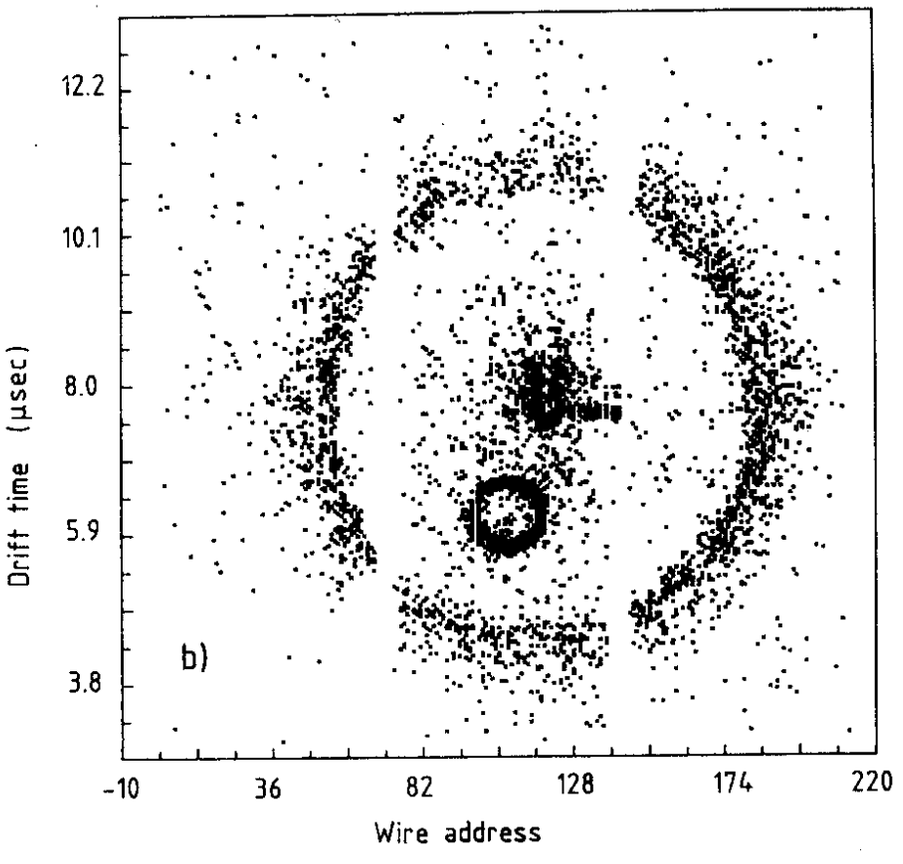
12.2
10.1
8.0
5.9
3.8
Drift time (µsec)
b)
-10
36
82
128
174
220
Wire address

Fig. 1

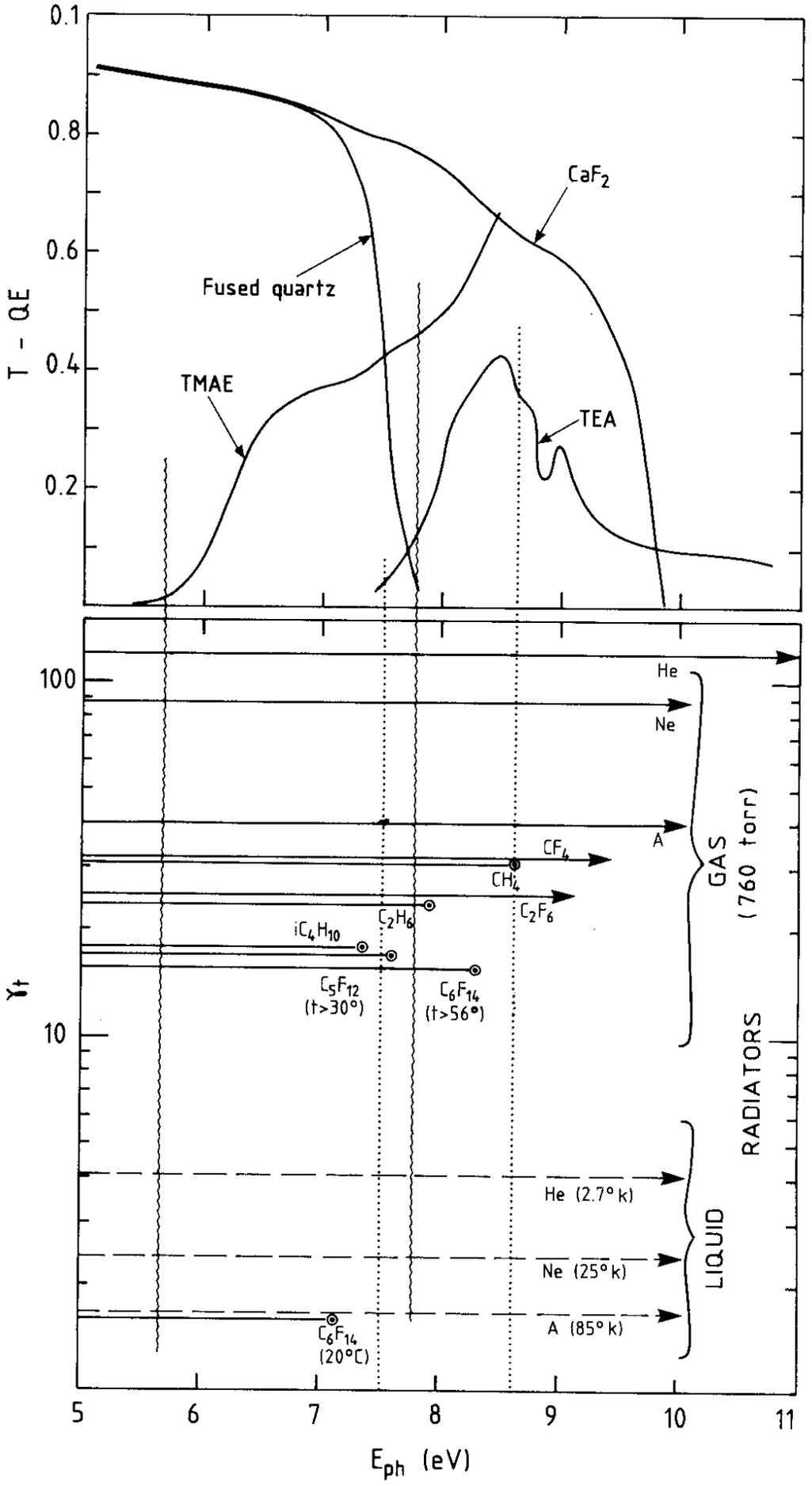
0.1
0.8
0.6
0.4
0.2
T - QE
CaF2
Fused quartz
TMAE
TEA
100
10
Yt
He
Ne
A
CF4
CH4
C2F6
C2H6
iC4H10
C5F12
(t>30°)
C6F14
(t>56°)
GAS
(760 torr)
RADIATORS
LIQUID
He (2.7° k)
Ne (25° k)
A (85° k)
C6F14
(20°C)
5
6
7
8
9
10
11
Eph (eV)

Fig. 2

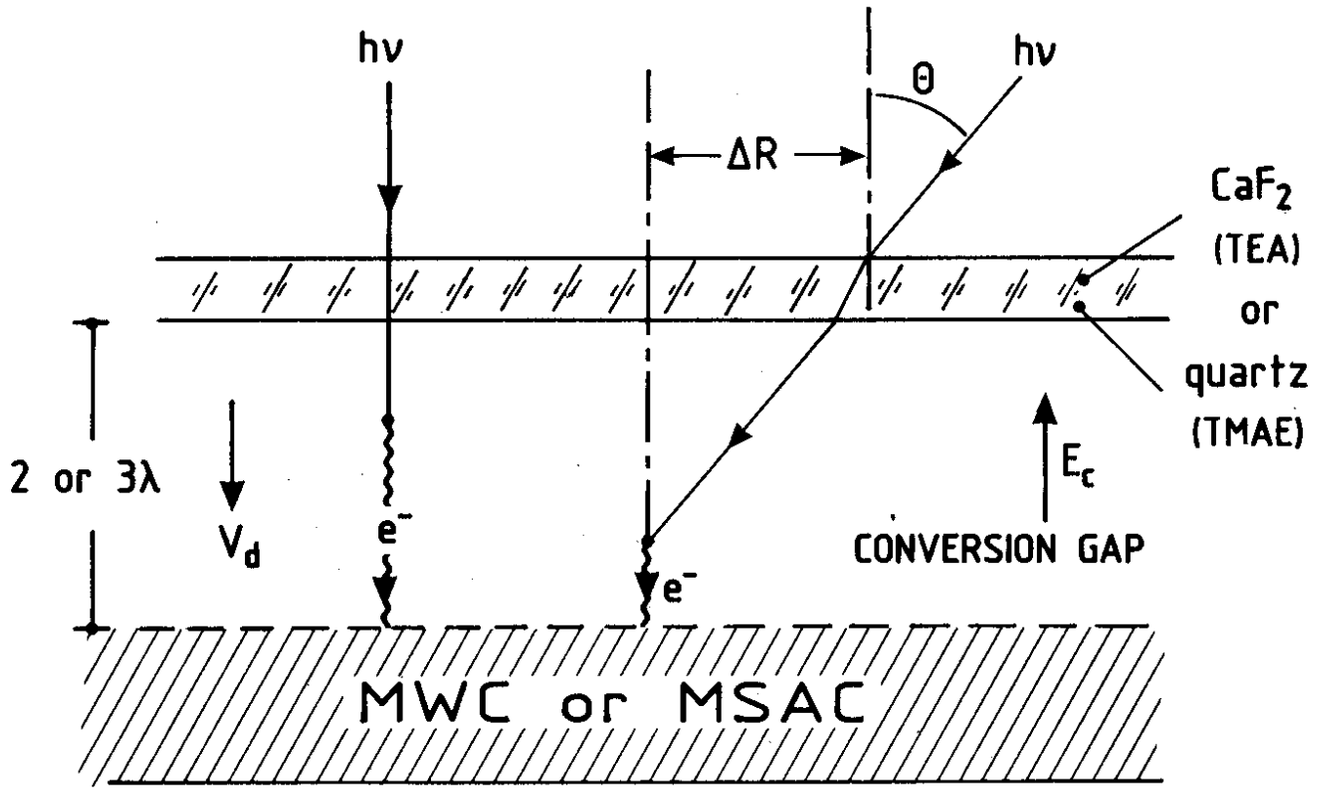
hν
hν
θ
ΔR
CaF2
(TEA)
or
quartz
(TMAE)
2 or 3λ
Vd
e⁻
e⁻
Ec
CONVERSION GAP
MWC or MSAC

Fig. 3

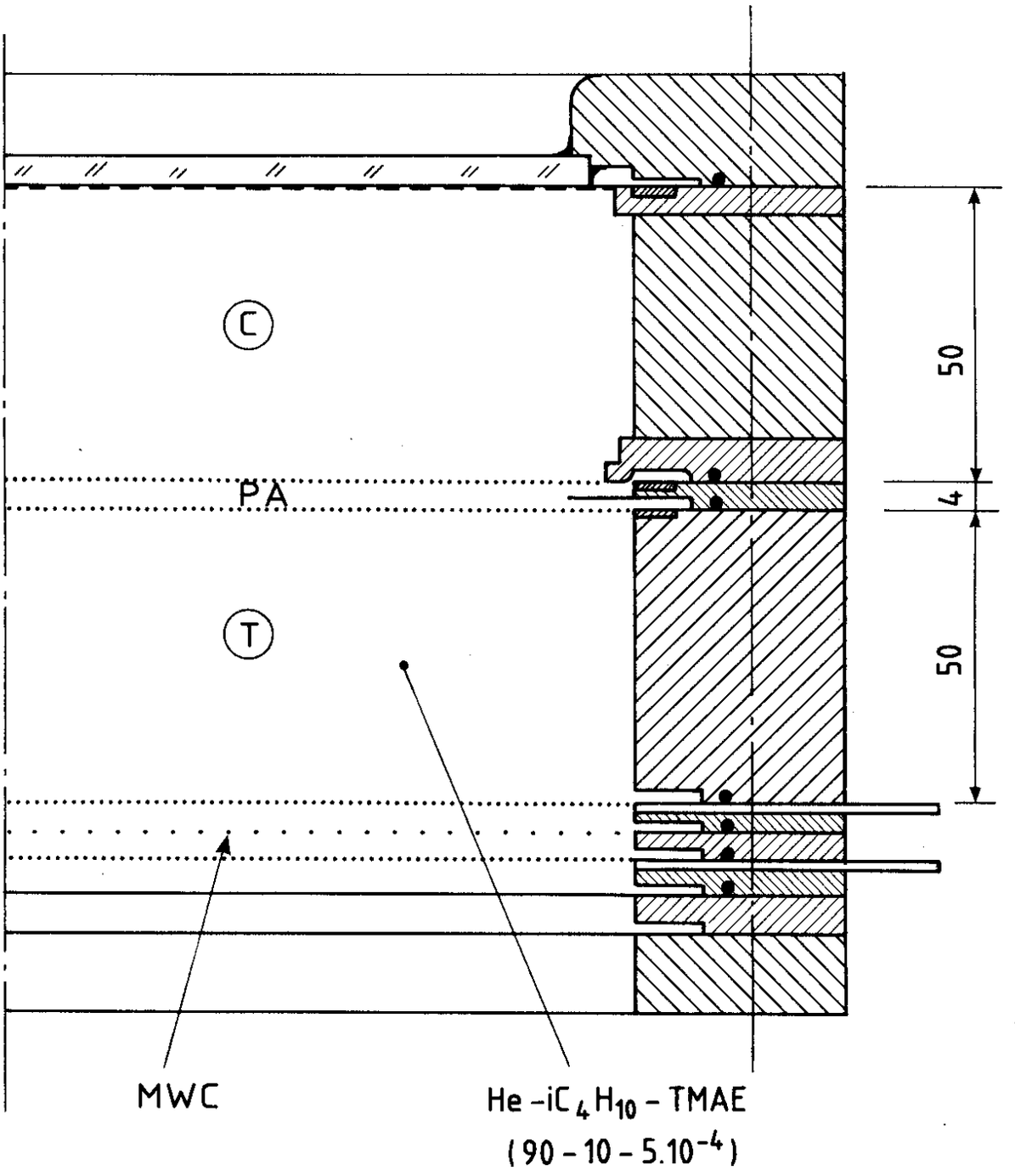

MULTISTEP AVALANCHE CHAMBER

Fig. 4

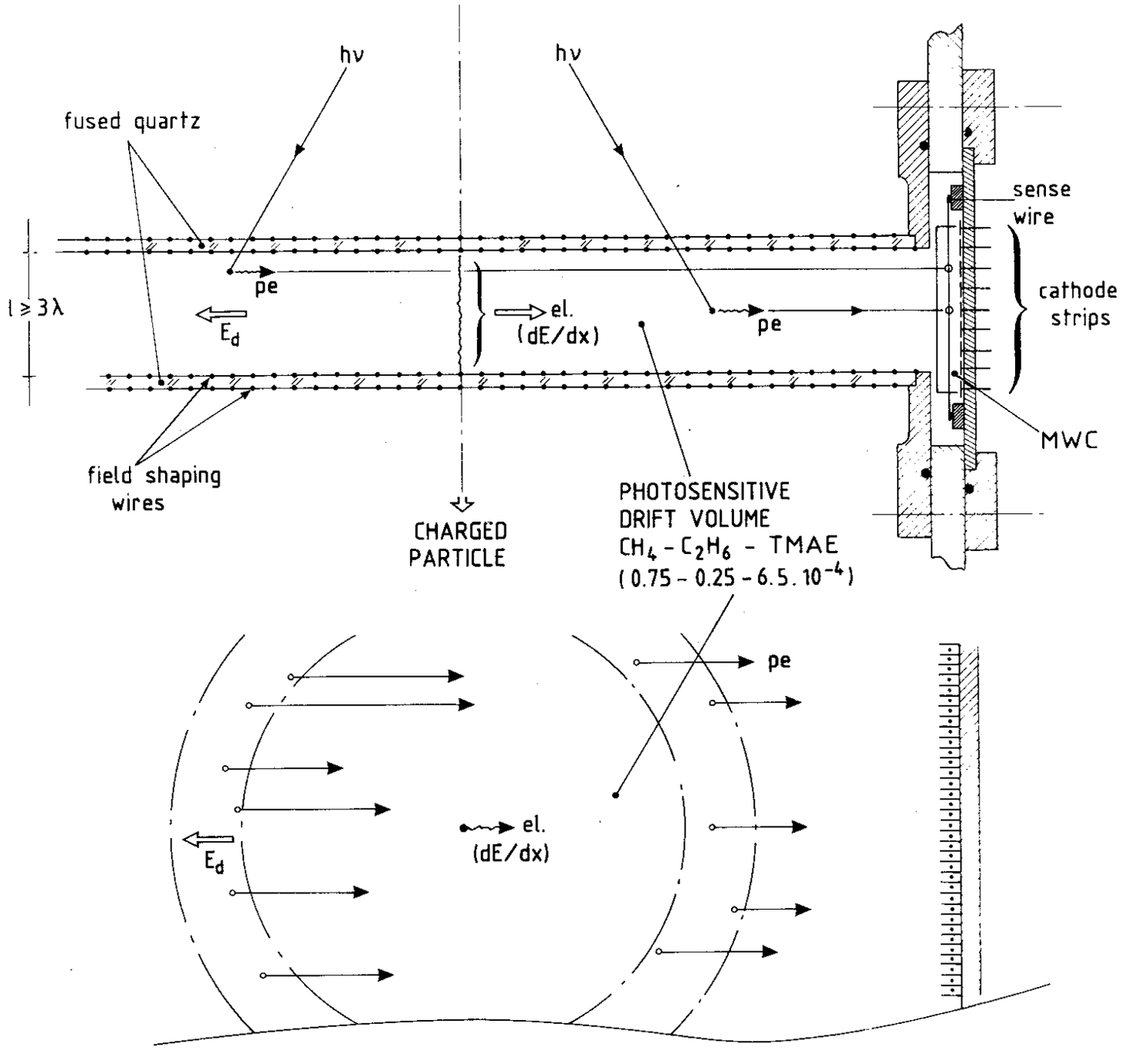
hν
hν
fused quartz
sense wire
pe
l ≥ 3λ
E_d
el. (dE/dx)
pe
cathode strips
MWC
field shaping wires
CHARGED PARTICLE
PHOTOSENSITIVE DRIFT VOLUME
CH4 - C2H6 - TMAE
(0.75 - 0.25 - 6.5.10^-4)
pe
el. (dE/dx)
E_d

Fig. 5

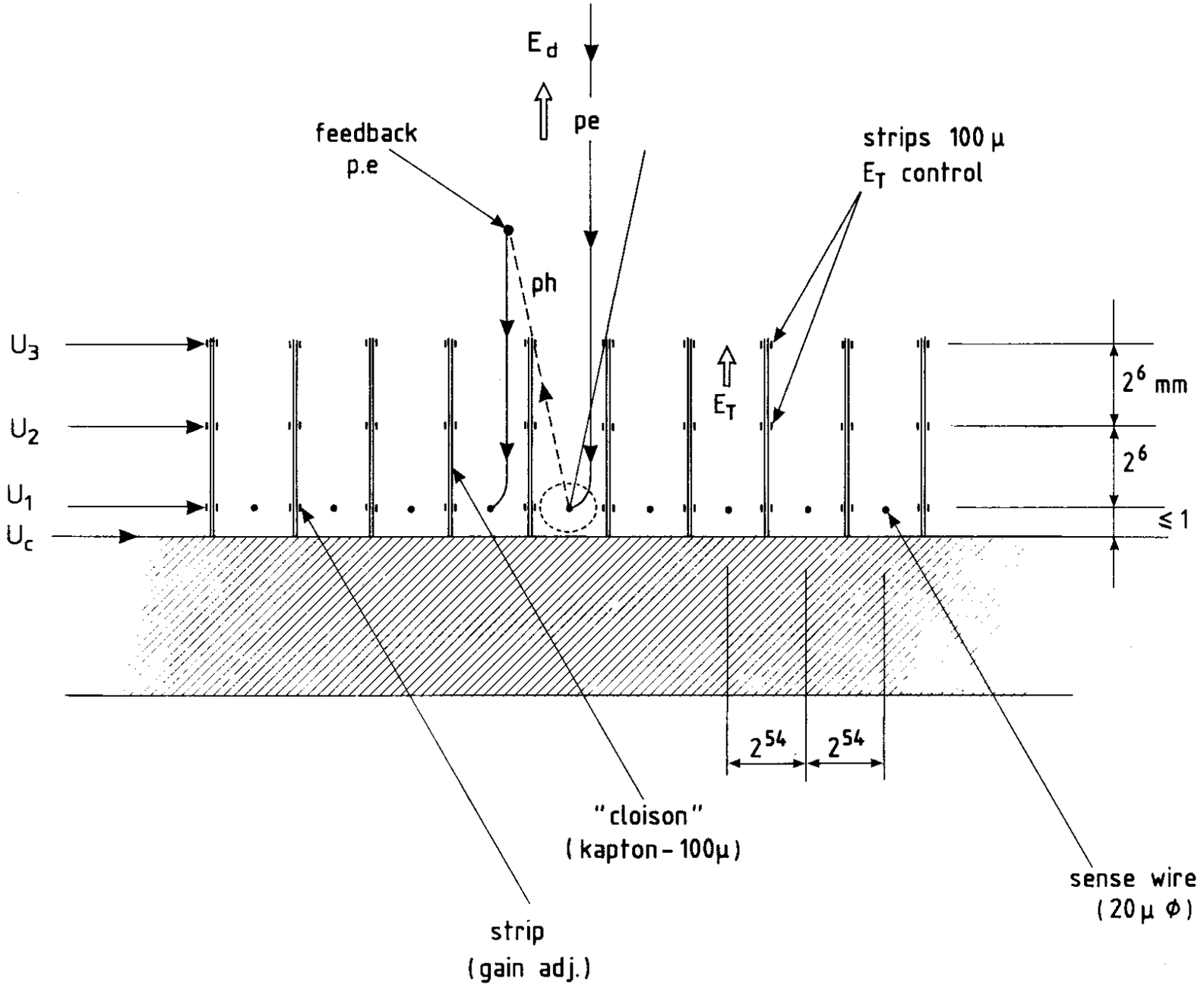
E_d
pe
feedback
p.e
ph
strips 100 µ
E_T control
U_3
U_2
U_1
U_c
E_T
2^6 mm
2^6
≦ 1
2^{54}
2^{54}
"cloison"
(kapton - 100µ)
sense wire
(20 µ φ)
strip
(gain adj.)

Fig. 6

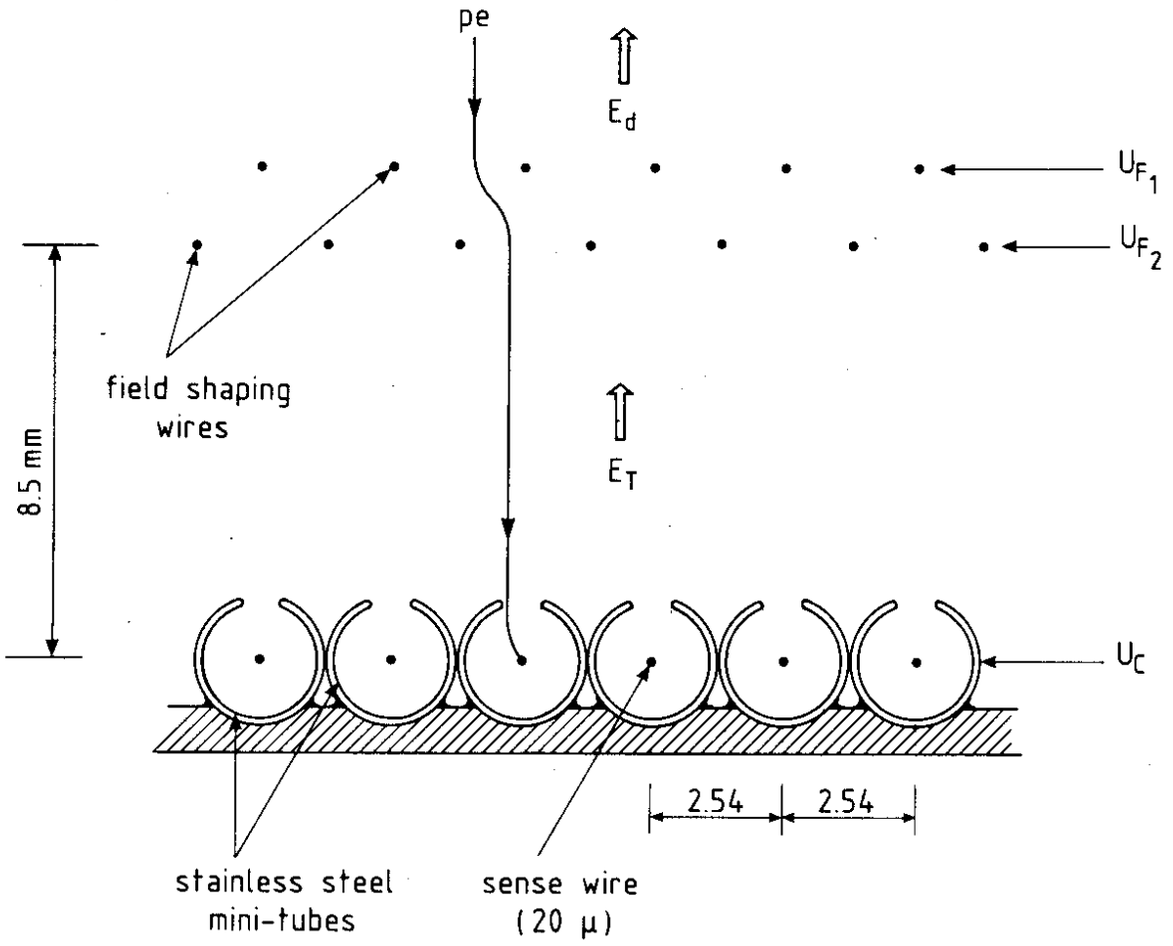
pe
E_d
U_{F_1}
U_{F_2}
field shaping
wires
8.5 mm
E_T
U_C
2.54
2.54
stainless steel
mini-tubes
sense wire
(20 μ)

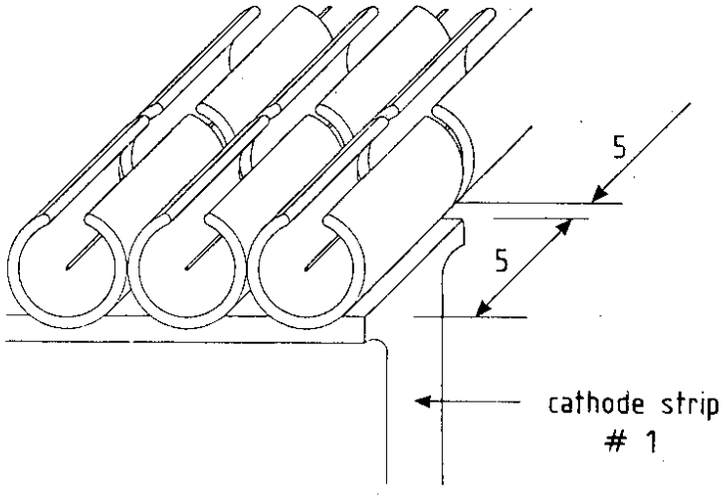
5
5
cathode strip
1

Fig. 7

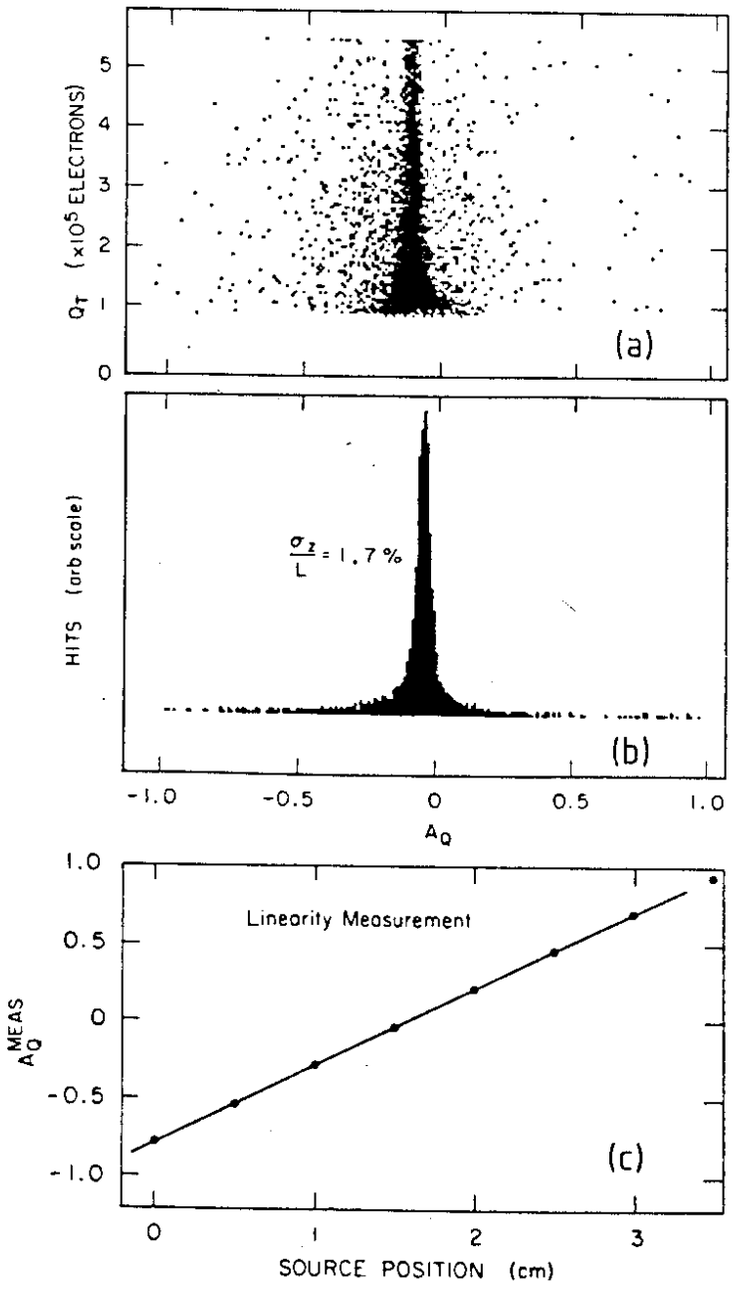
Q_T ($\times 10^5$ ELECTRONS)
5
4
3
2
1
0
(a)
HITS (arb scale)
$\frac{\sigma_z}{L} = 1.7\%$
(b)
-1.0
-0.5
0
0.5
1.0
A_Q
A_Q^{MEAS}
1.0
0.5
0
-0.5
-1.0
Linearity Measurement
(c)
0
1
2
3
SOURCE POSITION (cm)

Fig. 8

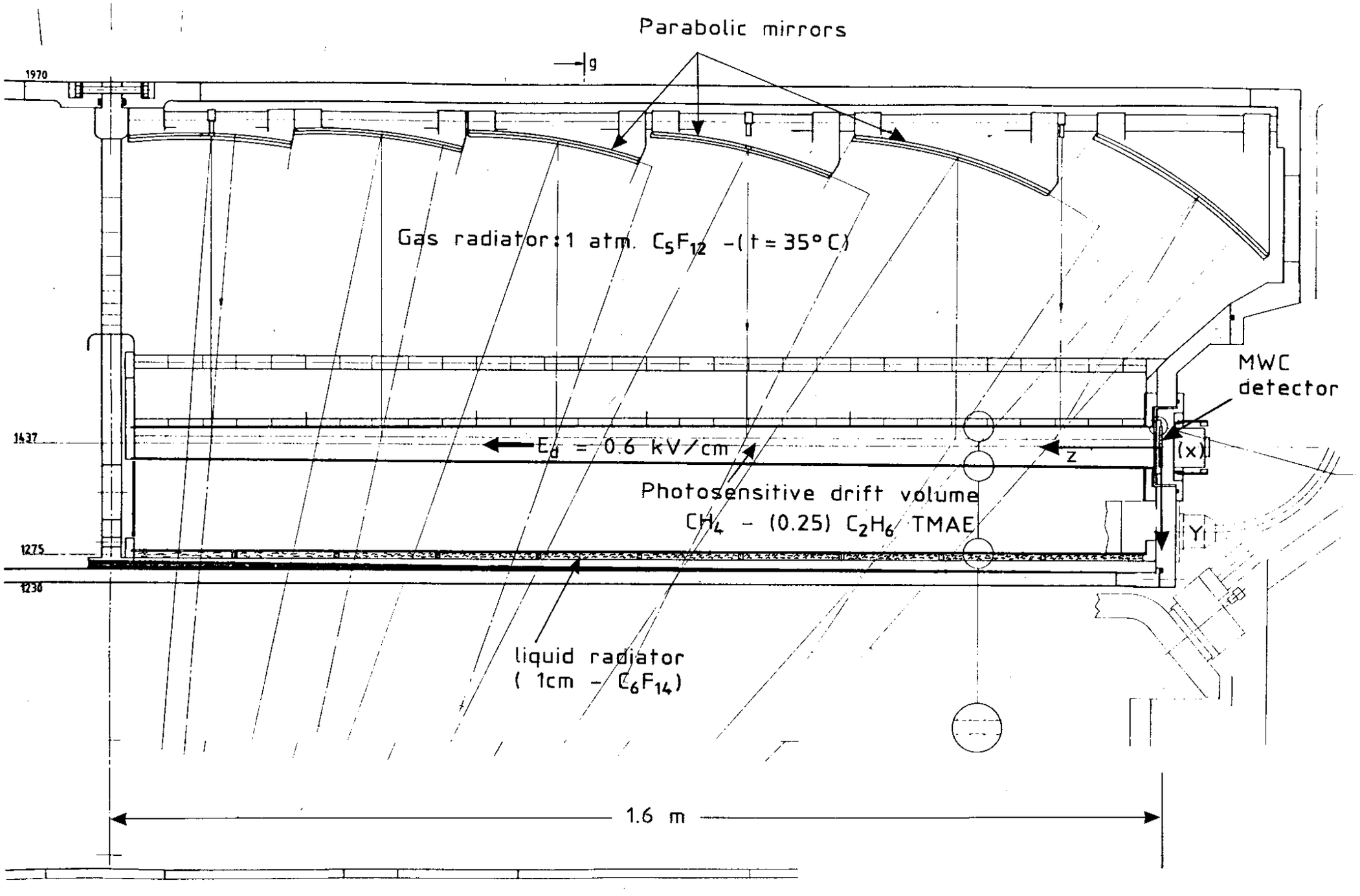
Parabolic mirrors
g
1970
Gas radiator: 1 atm. C_5F_{12} - (t = 35° C)
MWC detector
1437
E_d = 0.6 kV/cm
z
(x)
Photosensitive drift volume
CH_4 - (0.25) C_2H_6 TMAE
Y
1275
1230
liquid radiator
(1cm - C_6F_{14})
1.6 m

Fig. 9

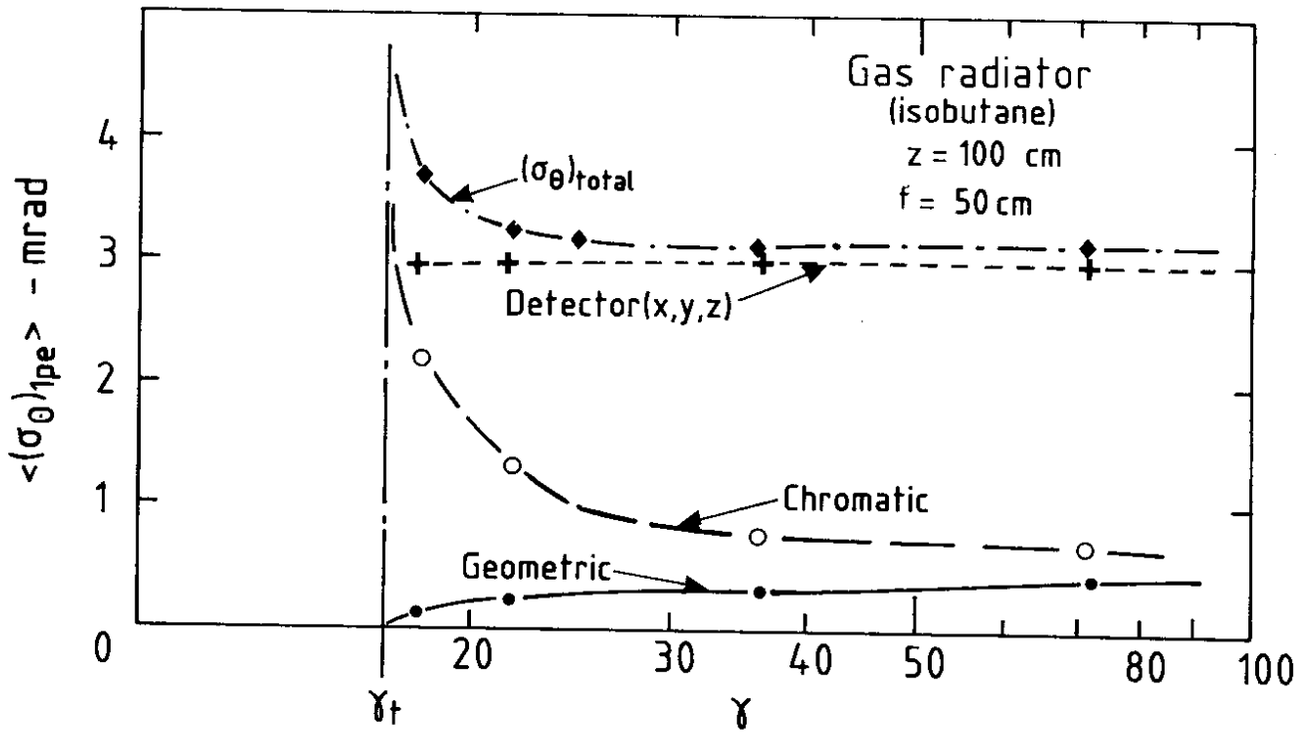
Gas radiator
(isobutane)
z = 100 cm
f = 50 cm
$(\sigma_\theta)_{total}$
Detector(x,y,z)
Chromatic
Geometric
$<(\sigma_\theta)_{1pe}>$ - mrad
γ_t
γ

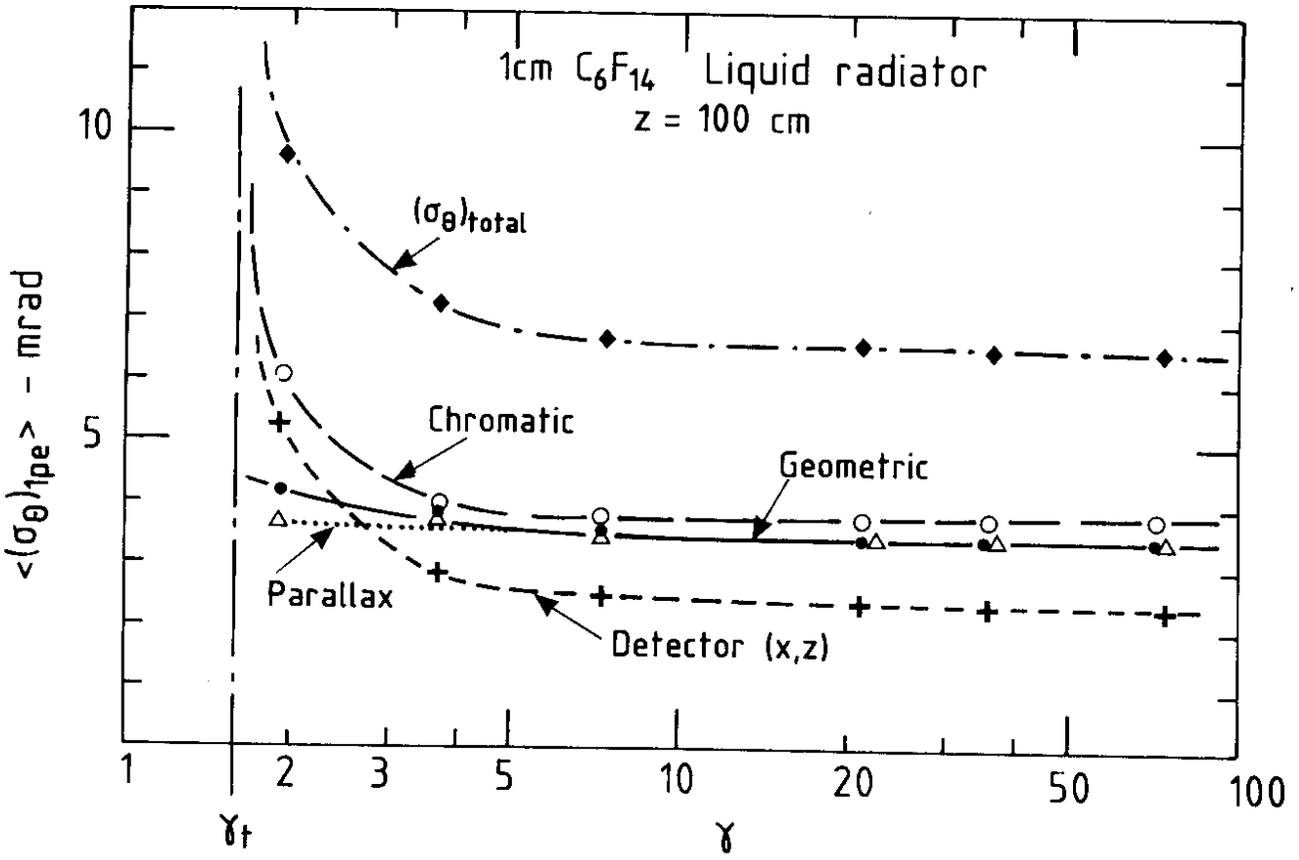
1cm C_6F_{14} Liquid radiator
z = 100 cm
$(\sigma_\theta)_{total}$
Chromatic
Geometric
Parallax
Detector (x,z)
$<(\sigma_\theta)_{1pe}>$ - mrad
γ_t
γ

Fig. 10

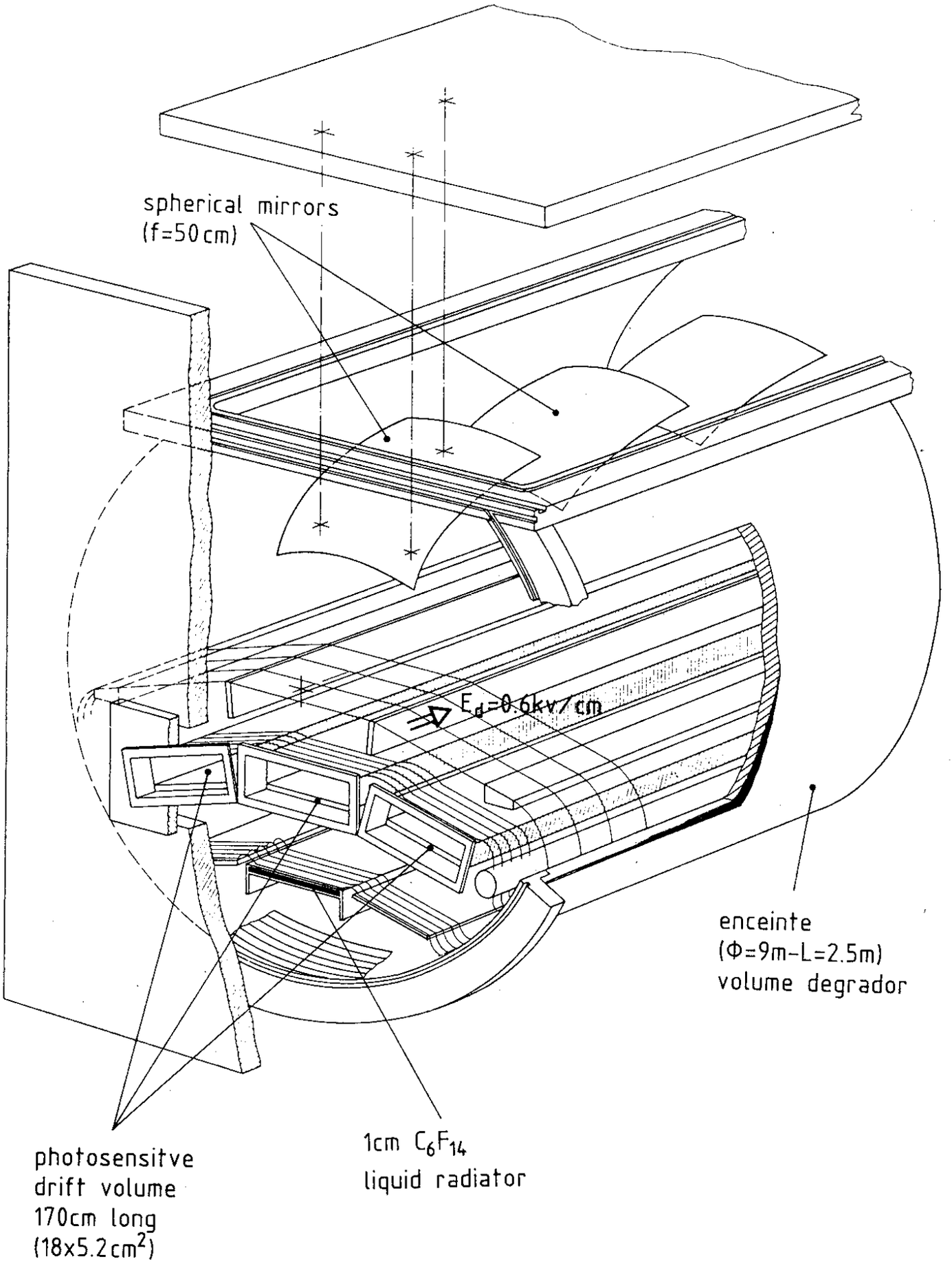
spherical mirrors
(f=50 cm)
E_d=0.6kv/cm
enceinte
(Φ=9m-L=2.5m)
volume degrador
photosensitve
drift volume
170cm long
(18x5.2 cm^2)
1cm C_6F_{14}
liquid radiator

Fig. 11

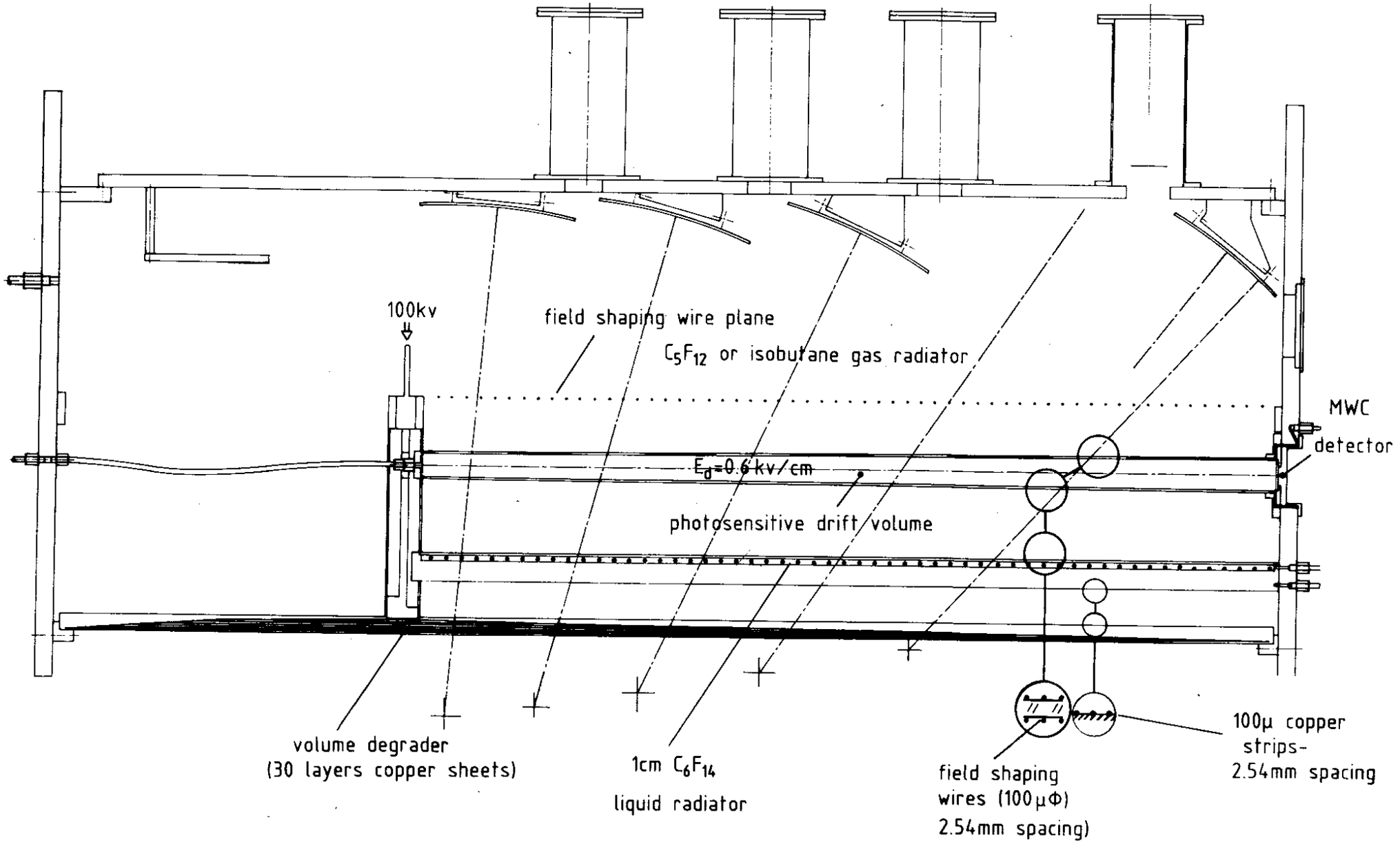
100kv
field shaping wire plane
C_5F_{12} or isobutane gas radiator
MWC
detector
E_d=0.6 kv/cm
photosensitive drift volume
volume degrader
(30 layers copper sheets)
1cm C_6F_{14}
liquid radiator
field shaping
wires (100 μΦ)
2.54mm spacing)
100μ copper
strips-
2.54mm spacing

Fig. 12

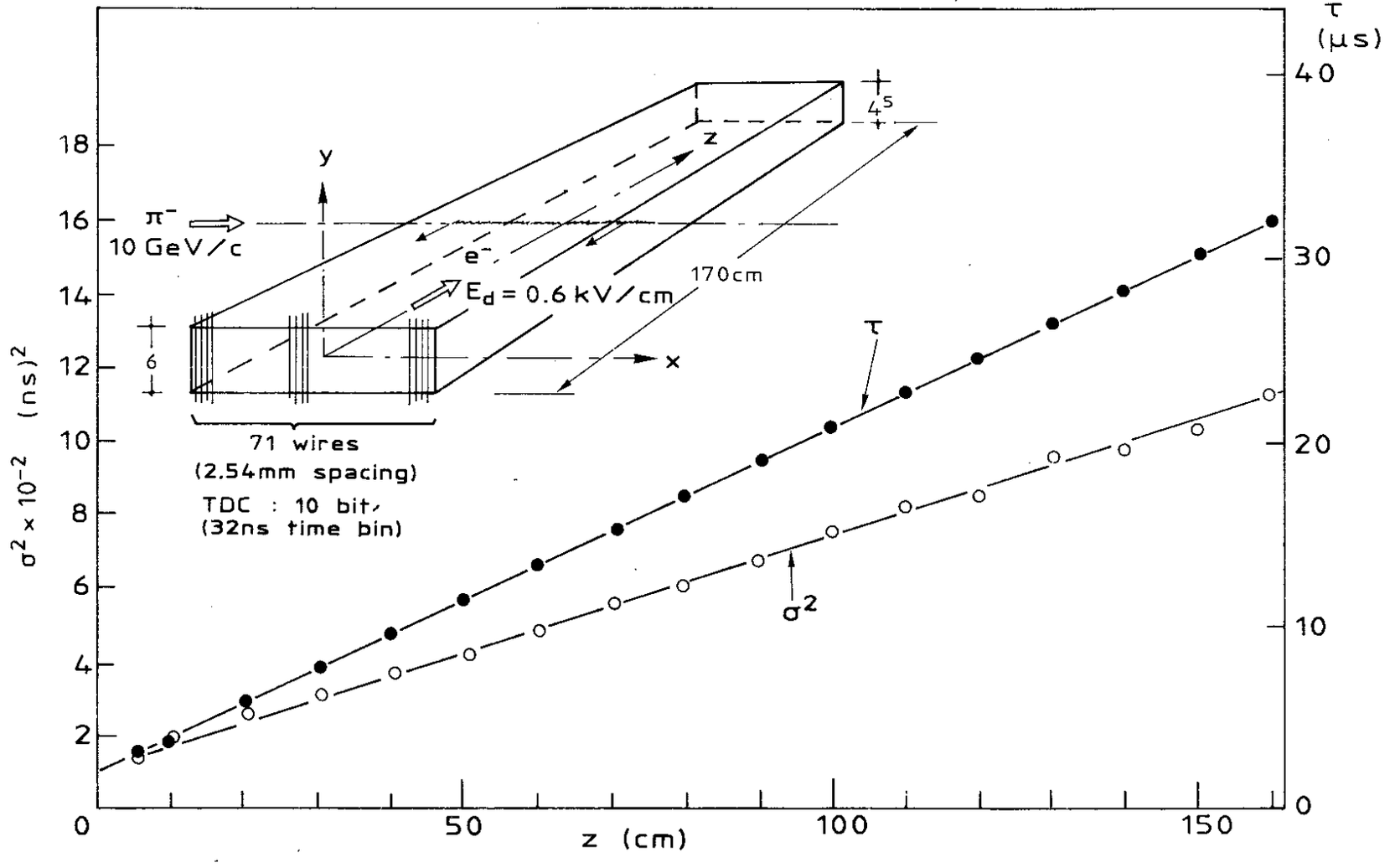
τ (μs)
$\sigma^2 \times 10^{-2}$ (ns)^2
z (cm)
π⁻
10 GeV/c
e⁻
E_d = 0.6 kV/cm
170cm
4.5
6
71 wires
(2.54mm spacing)
TDC : 10 bit
(32ns time bin)
τ
σ^2
x
y
z

Fig. 13

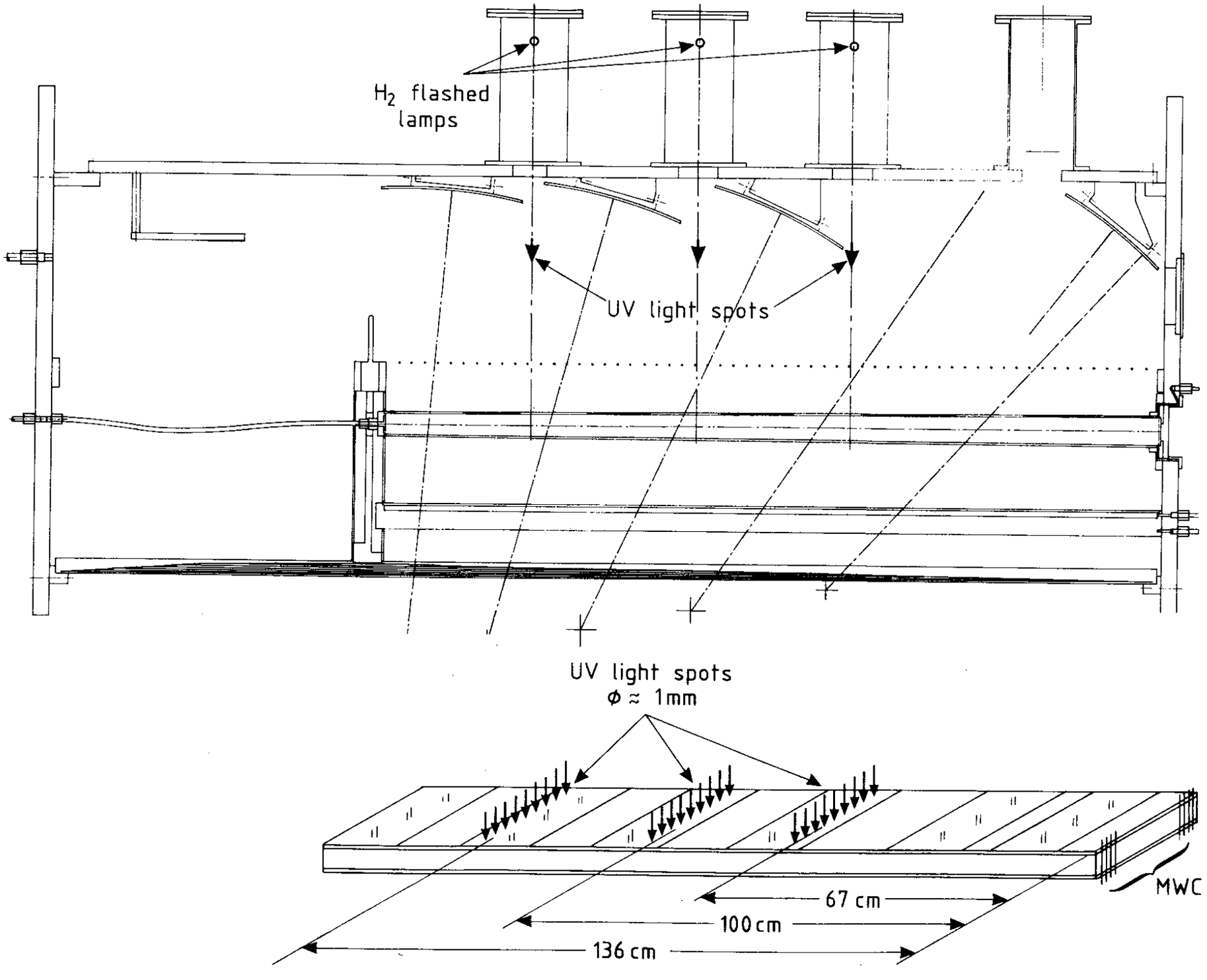
H_2 flashed lamps
UV light spots
UV light spots
$\phi \approx$ 1mm
67 cm
100 cm
136 cm
MWC

Fig. 14

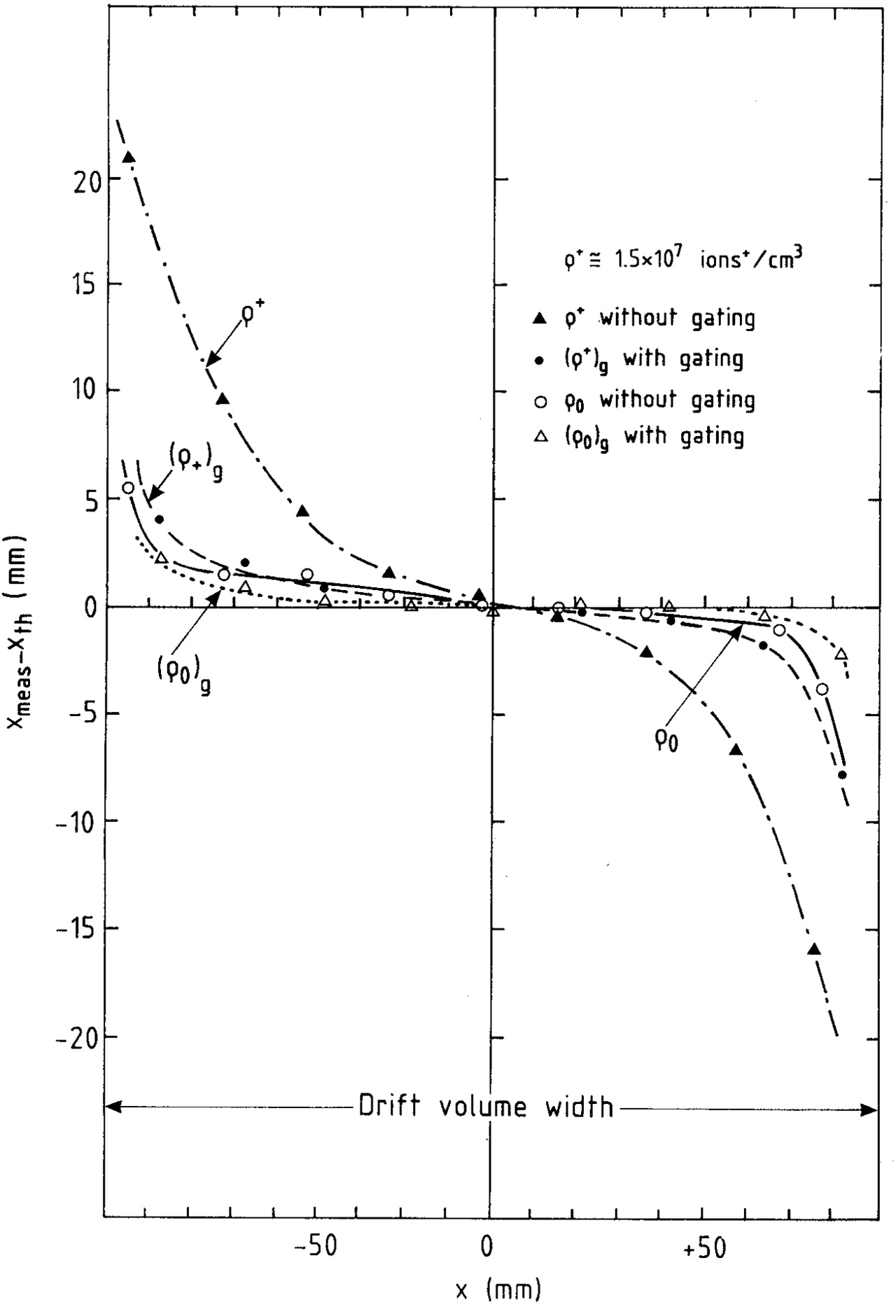
$\rho^+ \cong 1.5\times10^7$ ions$^+$/cm^3
ρ^+ without gating
$(\rho^+)_g$ with gating
ρ_0 without gating
$(\rho_0)_g$ with gating
ρ^+
$(\rho_+)_g$
$(\rho_0)_g$
ρ_0
Drift volume width
$x_{meas}-x_{th}$ (mm)
x (mm)
20
15
10
5
0
-5
-10
-15
-20
-50
0
+50

Fig. 15a

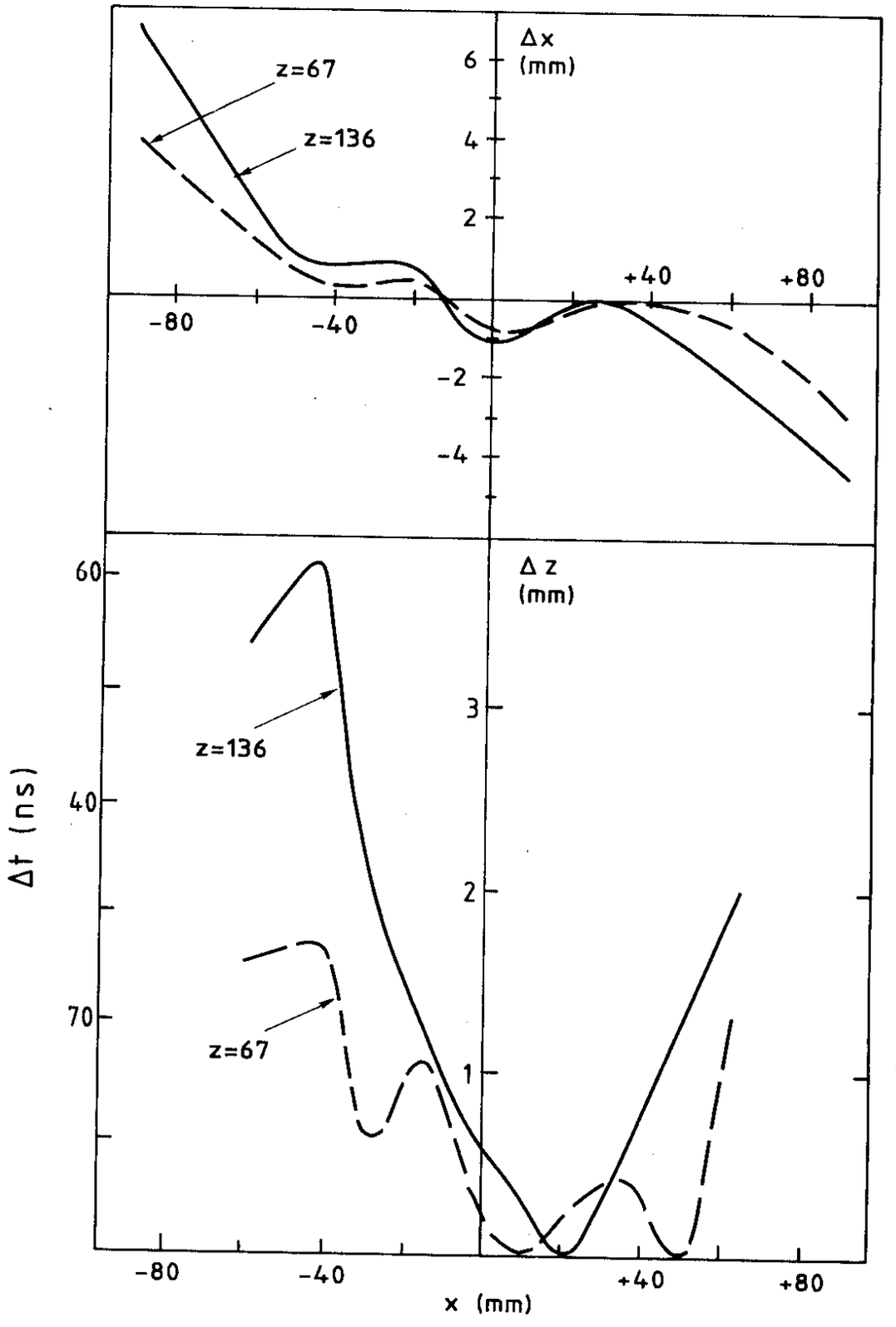
Δx
(mm)
z=67
z=136
6
4
2
-2
-4
-80
-40
+40
+80
Δz
(mm)
z=136
z=67
60
40
70
3
2
1
Δt (ns)
-80
-40
+40
+80
x (mm)

Fig. 15b

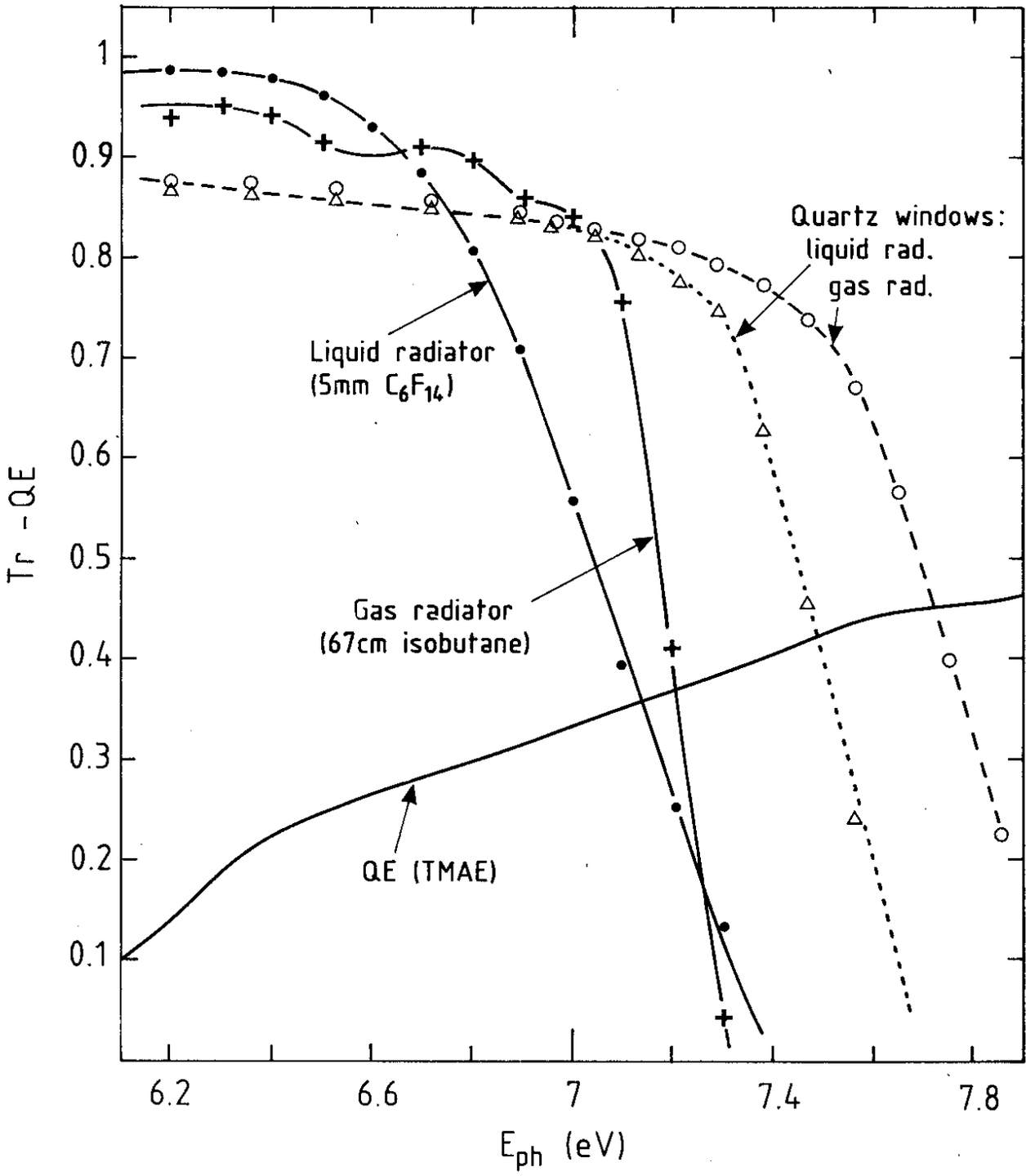
Tr - QE
1
0.9
0.8
0.7
0.6
0.5
0.4
0.3
0.2
0.1
6.2
6.6
7
7.4
7.8
E_{ph} (eV)
Quartz windows:
liquid rad.
gas rad.
Liquid radiator
(5mm C_6F_{14})
Gas radiator
(67cm isobutane)
QE (TMAE)

Fig. 16

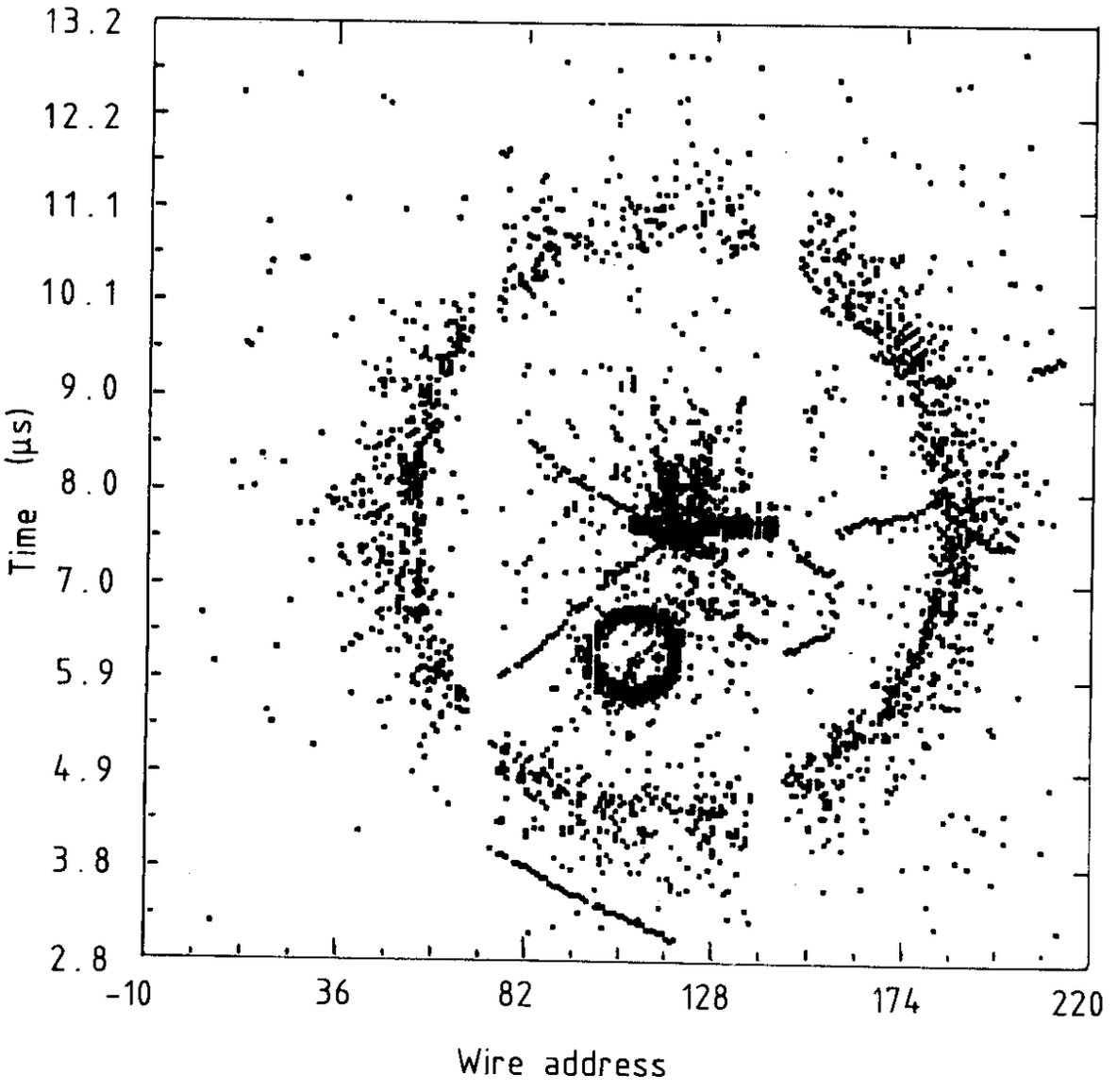
13.2
12.2
11.1
10.1
9.0
8.0
7.0
5.9
4.9
3.8
2.8
Time (μs)
-10
36
82
128
174
220
Wire address

Fig. 17

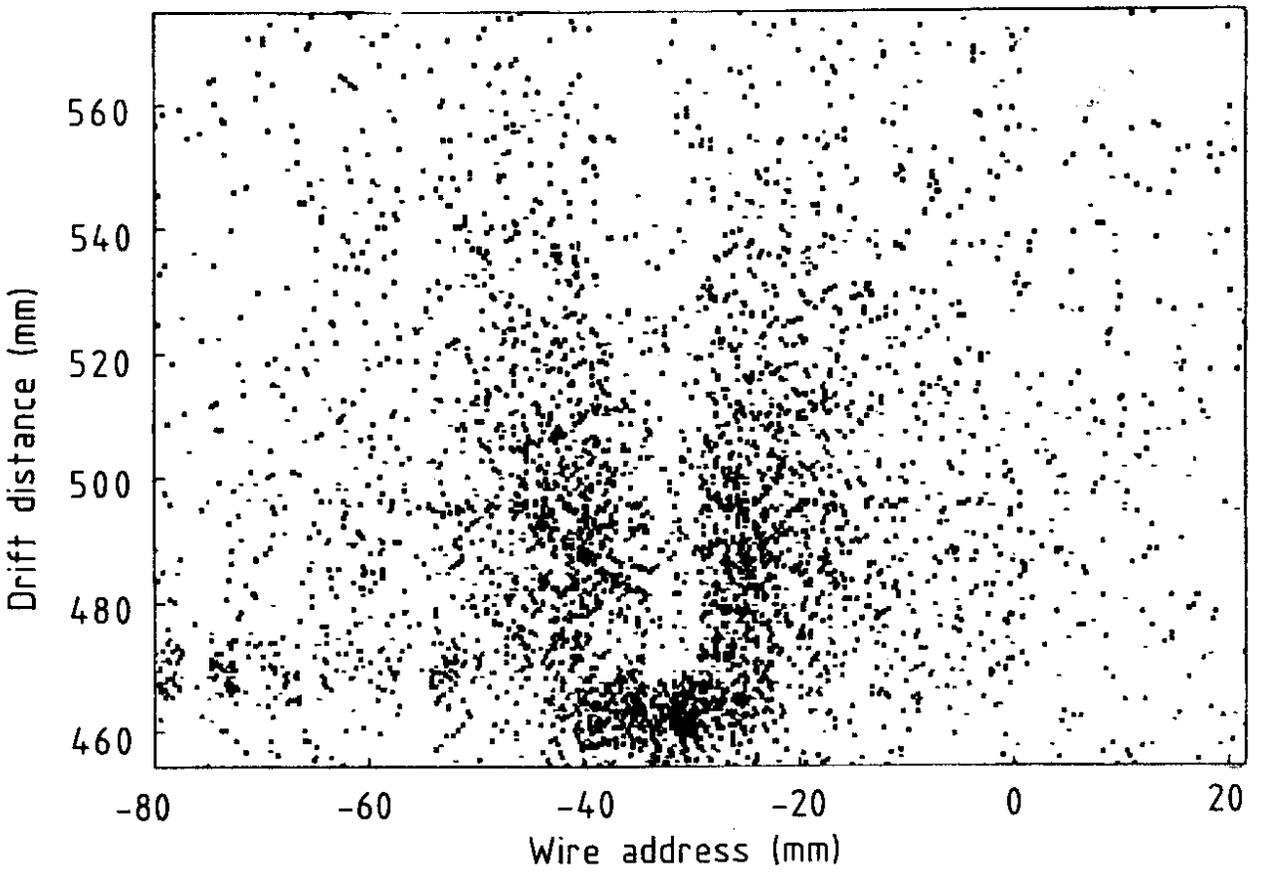
Drift distance (mm)
560
540
520
500
480
460
-80
-60
-40
-20
0
20
Wire address (mm)

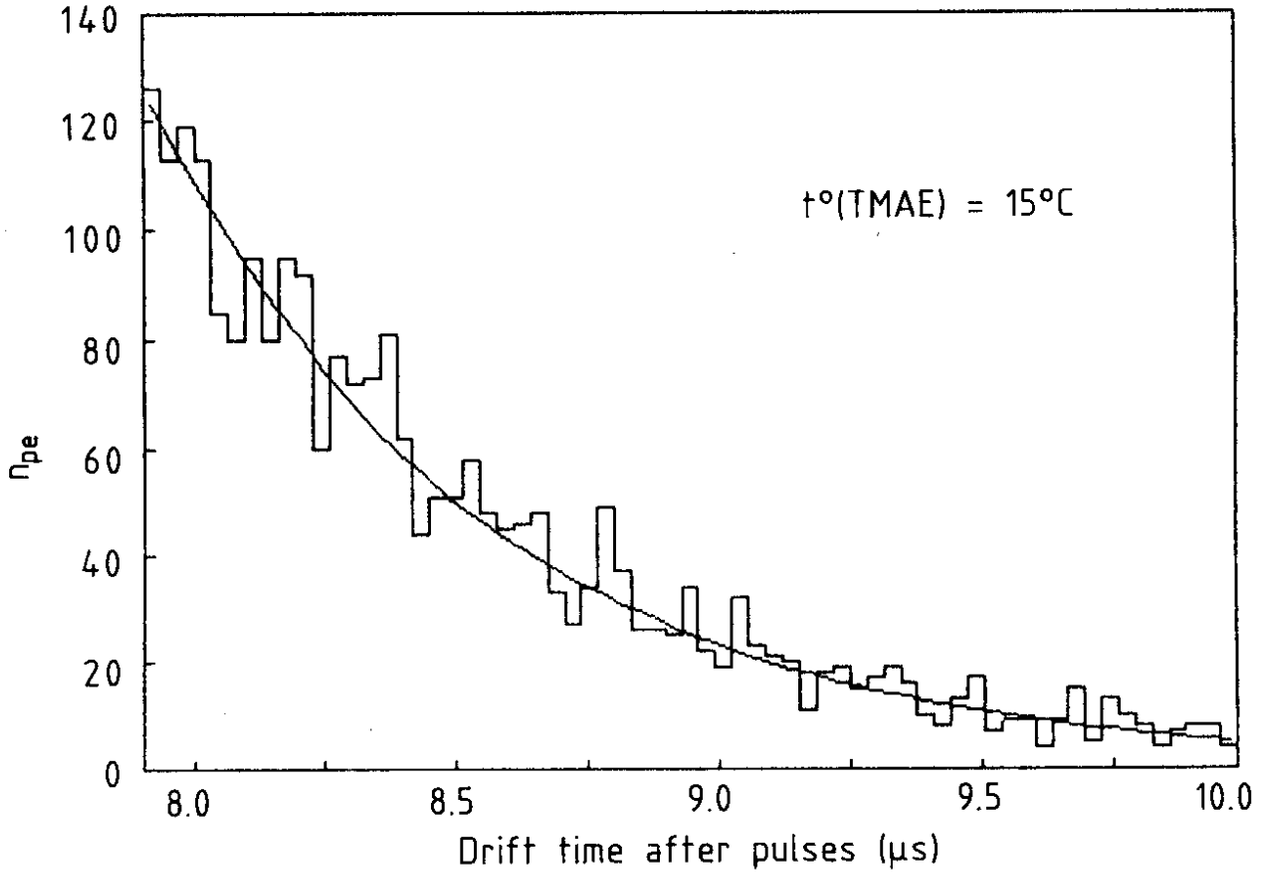
n_{pe}
140
120
100
80
60
40
20
0
t°(TMAE) = 15°C
8.0
8.5
9.0
9.5
10.0
Drift time after pulses (μs)

Fig. 18

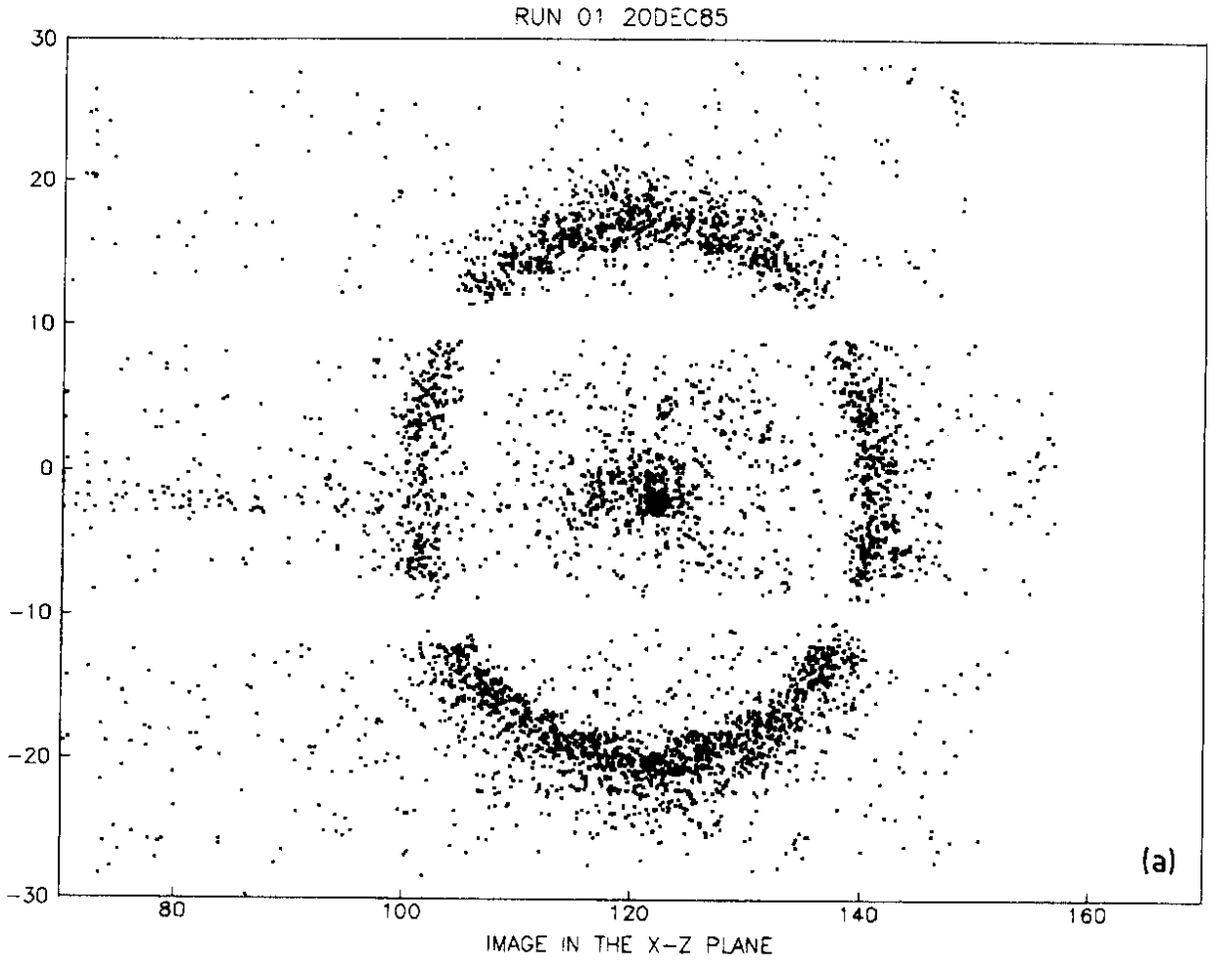
RUN 01 20DEC85
30
20
10
0
-10
-20
-30
80
100
120
140
160
(a)
IMAGE IN THE X-Z PLANE

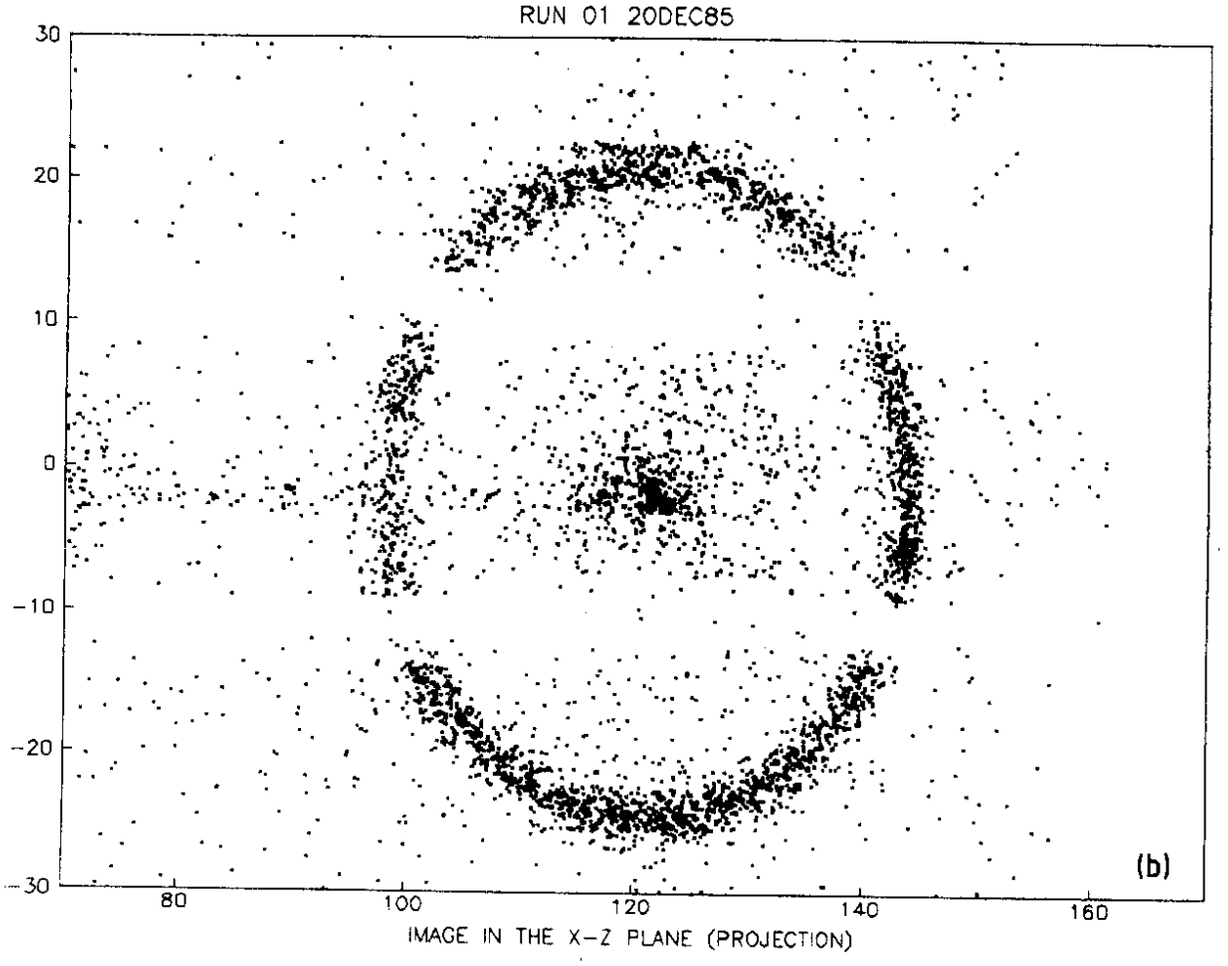
RUN 01 20DEC85
30
20
10
0
-10
-20
-30
80
100
120
140
160
(b)
IMAGE IN THE X-Z PLANE (PROJECTION)

Fig. 19

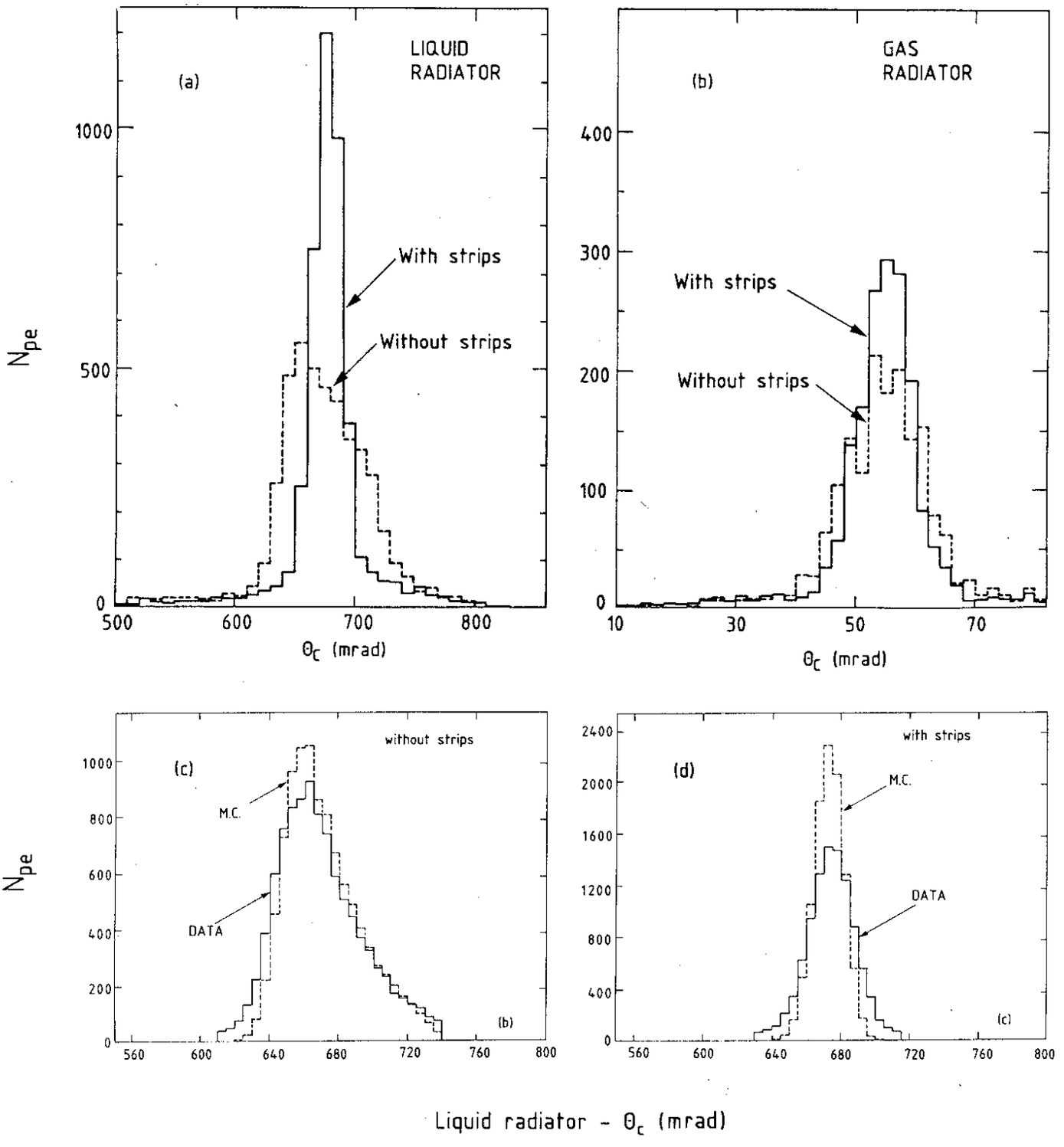
LIQUID
RADIATOR
(a)
With strips
Without strips
N_{pe}
θ_C (mrad)
GAS
RADIATOR
(b)
With strips
Without strips
θ_C (mrad)
without strips
(c)
M.C.
DATA
(b)
with strips
(d)
M.C.
DATA
(c)
Liquid radiator - θ_C (mrad)

Fig. 20

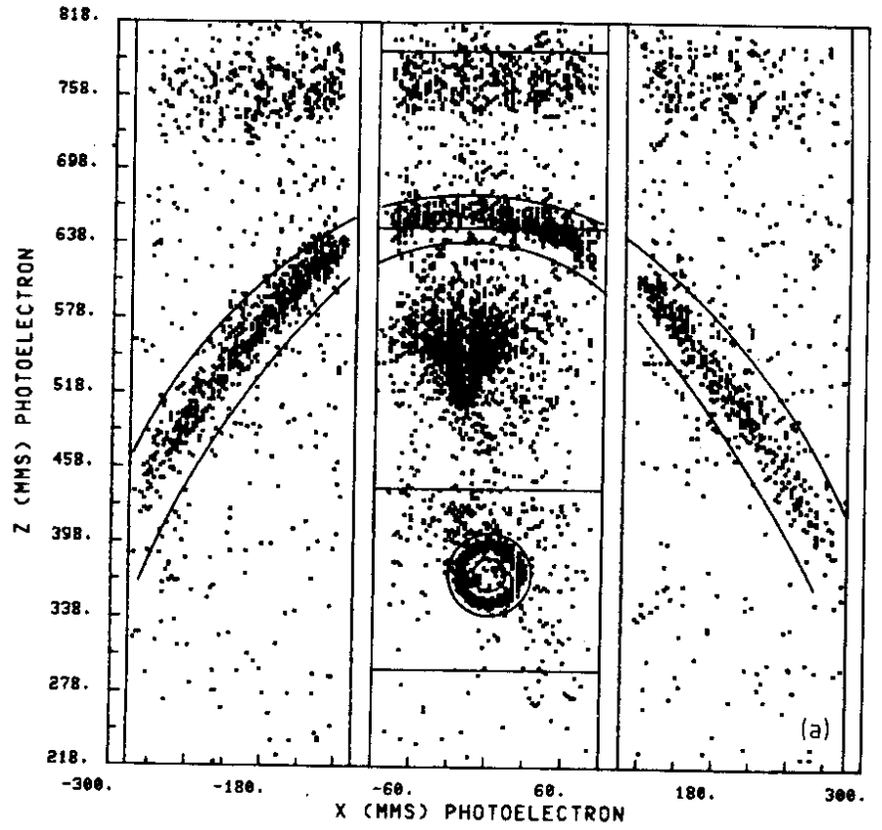

M.C. SIMULATION

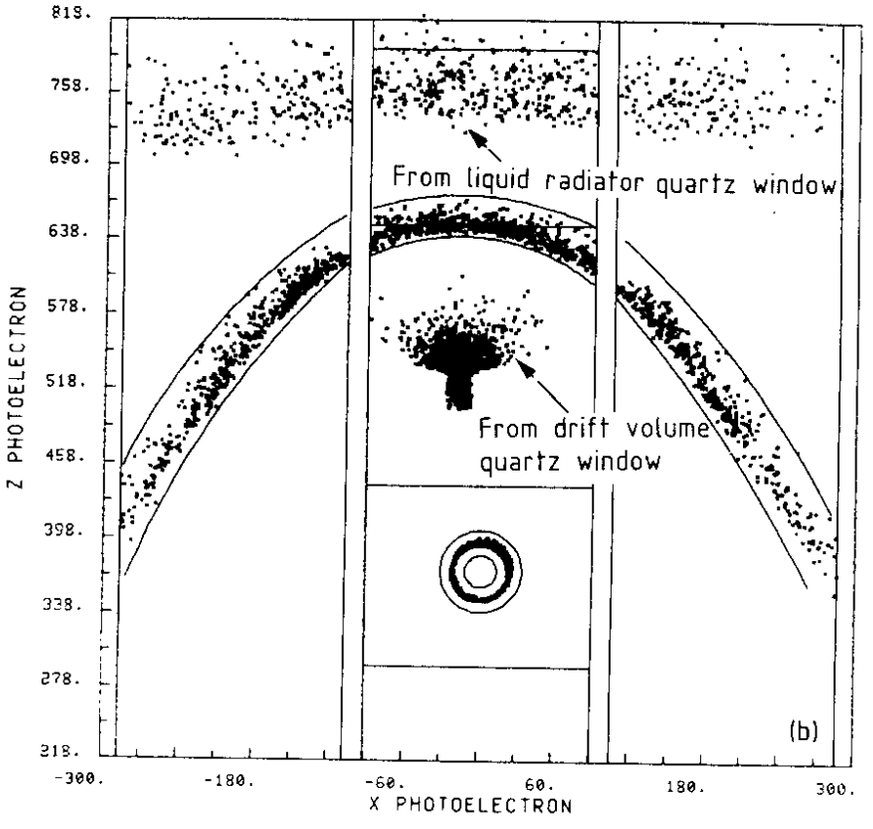

Fig. 21

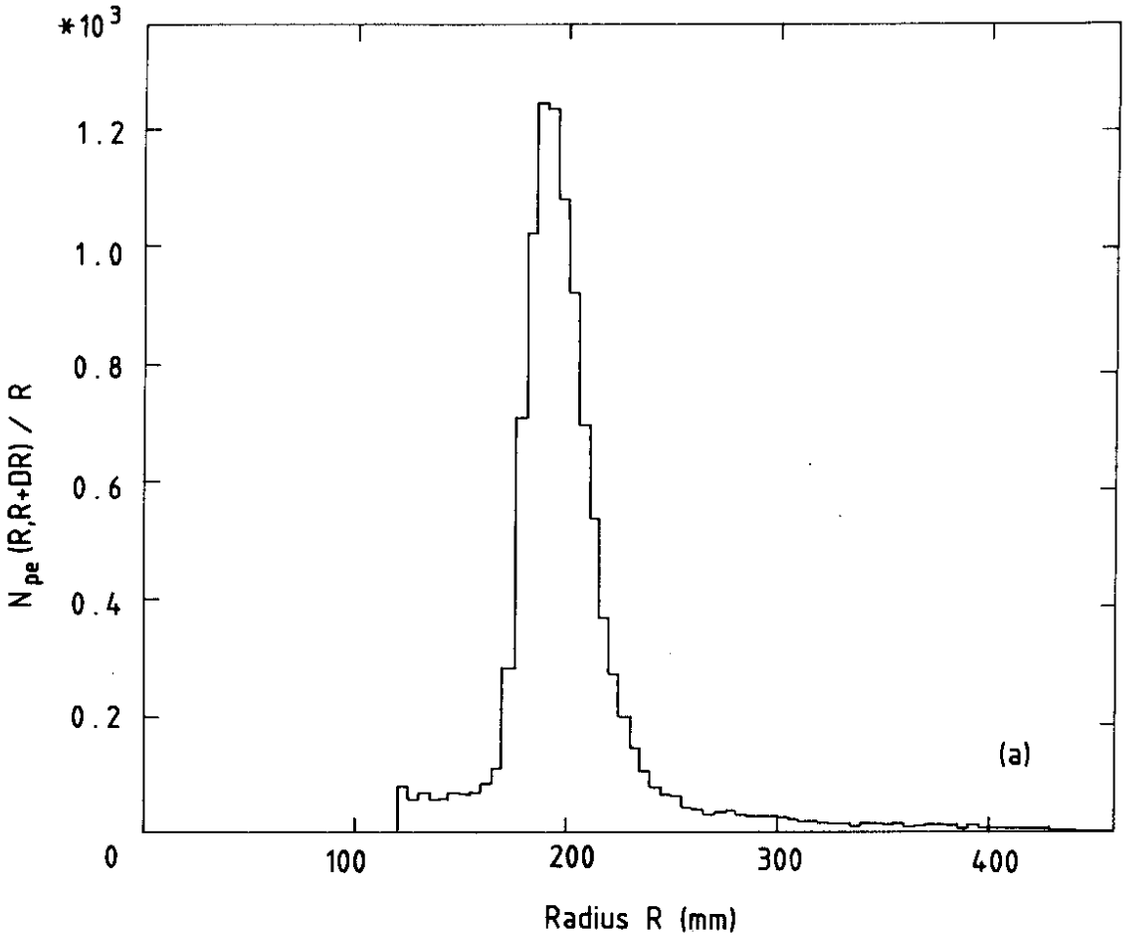
*10^3
1.2
1.0
0.8
0.6
0.4
0.2
0
N_pe (R,R+DR) / R
100
200
300
400
Radius R (mm)
(a)

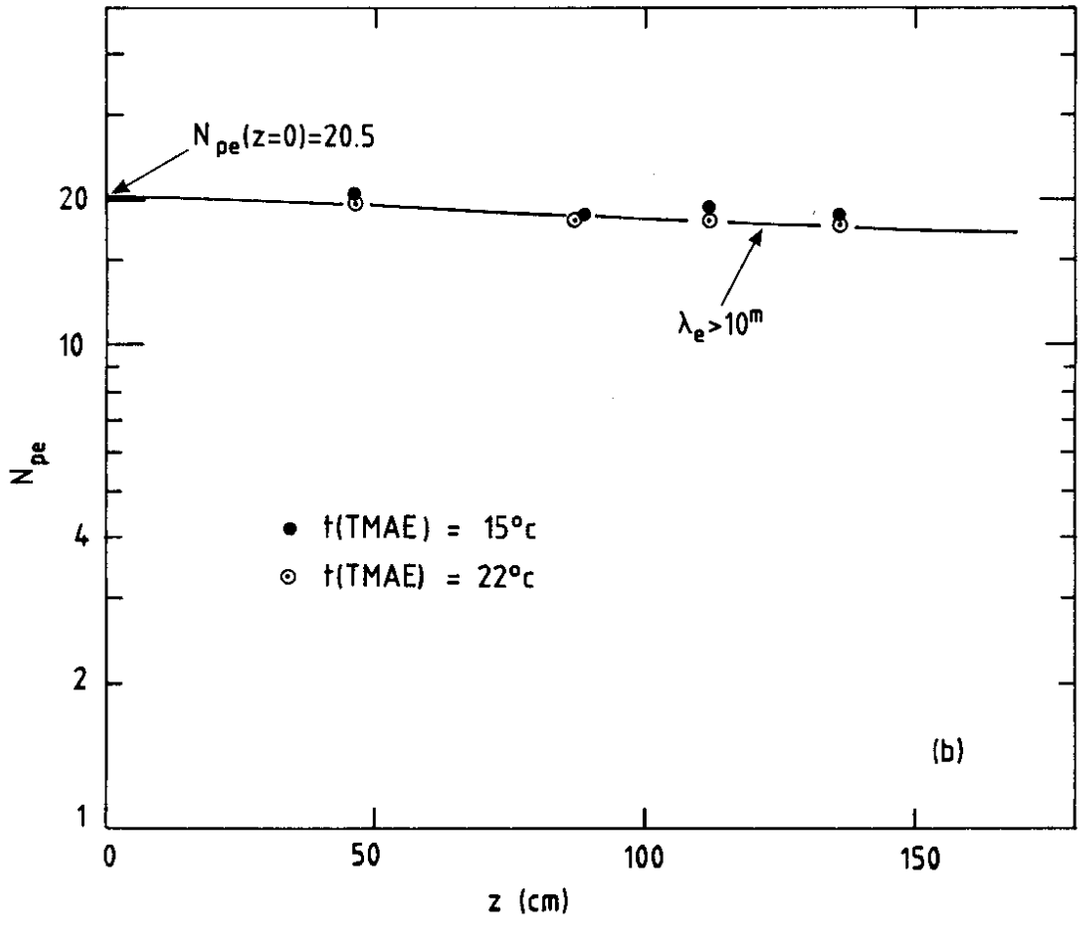
N_pe(z=0)=20.5
20
10
4
2
1
N_pe
λ_e>10^m
• t(TMAE) = 15°c
⊙ t(TMAE) = 22°c
(b)
0
50
100
150
z (cm)

Fig. 22

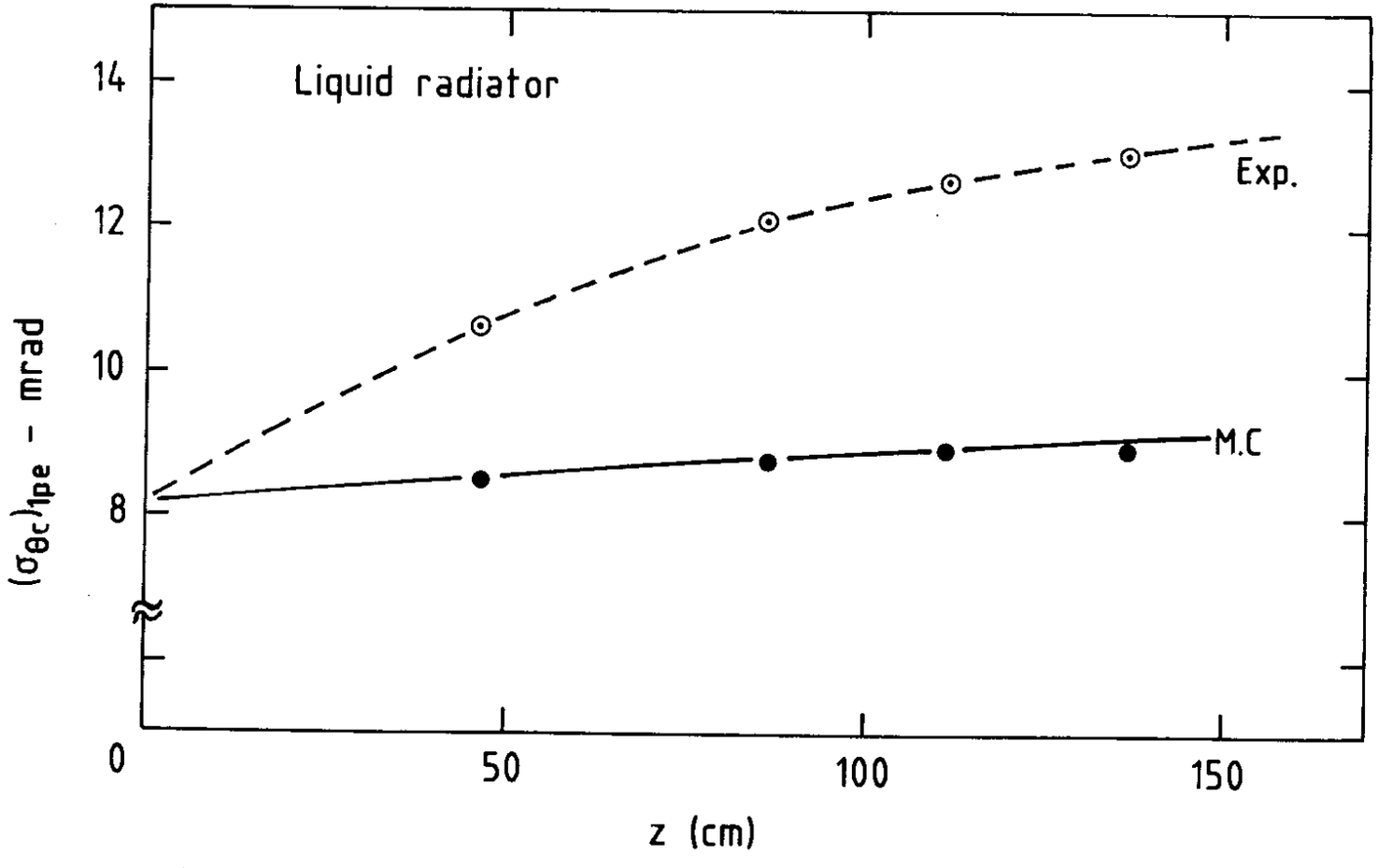
Liquid radiator
Exp.
M.C
14
12
10
8
0
50
100
150
z (cm)
$(\sigma_{\theta c})_{1pe}$ - mrad

Fig. 23

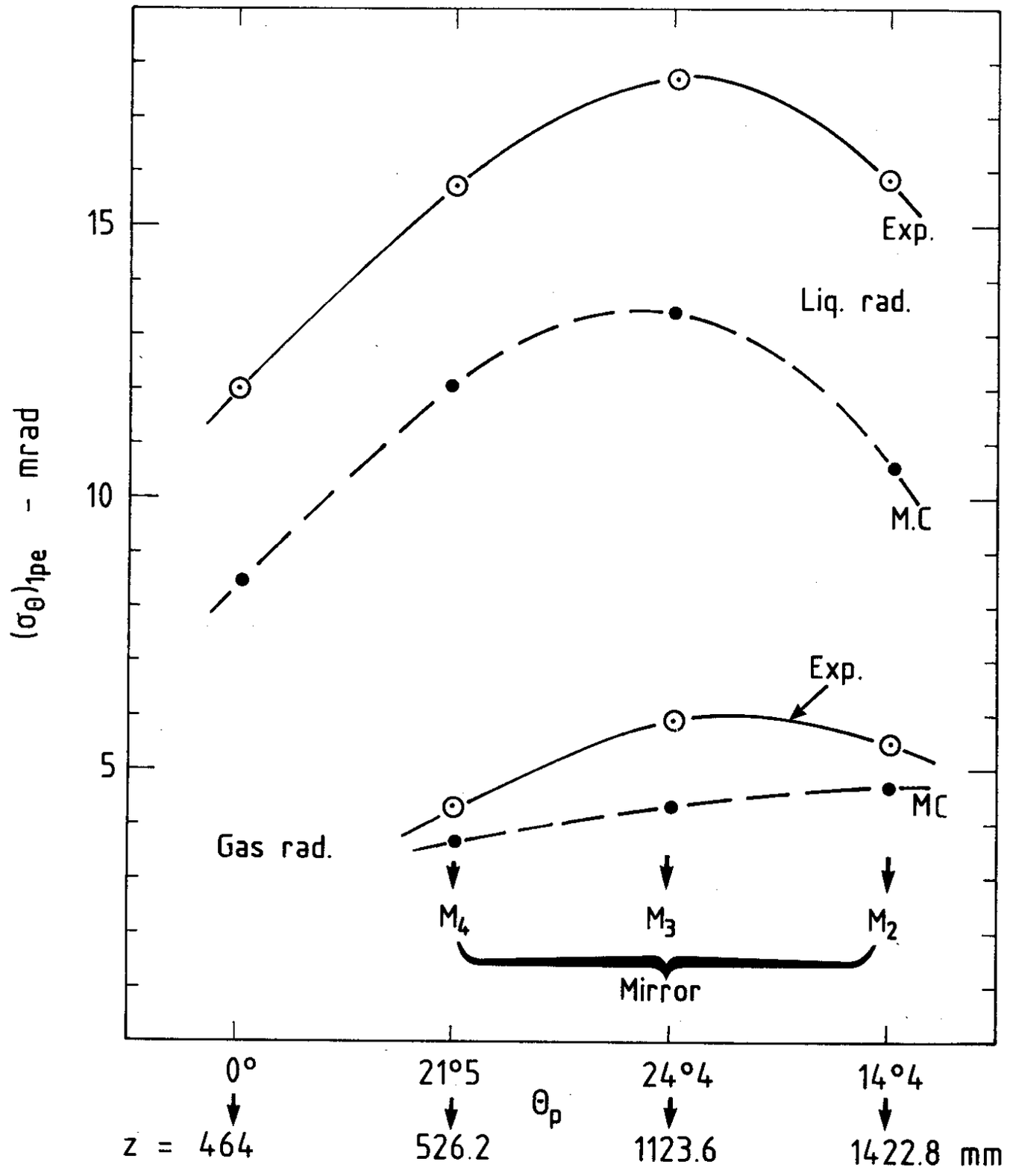
15
10
5
$(\sigma_\theta)_{1pe}$ - mrad
Exp.
Liq. rad.
M.C
Exp.
MC
Gas rad.
M_4
M_3
M_2
Mirror
0°
21°5
24°4
14°4
θ_p
z = 464
526.2
1123.6
1422.8 mm

Fig. 24

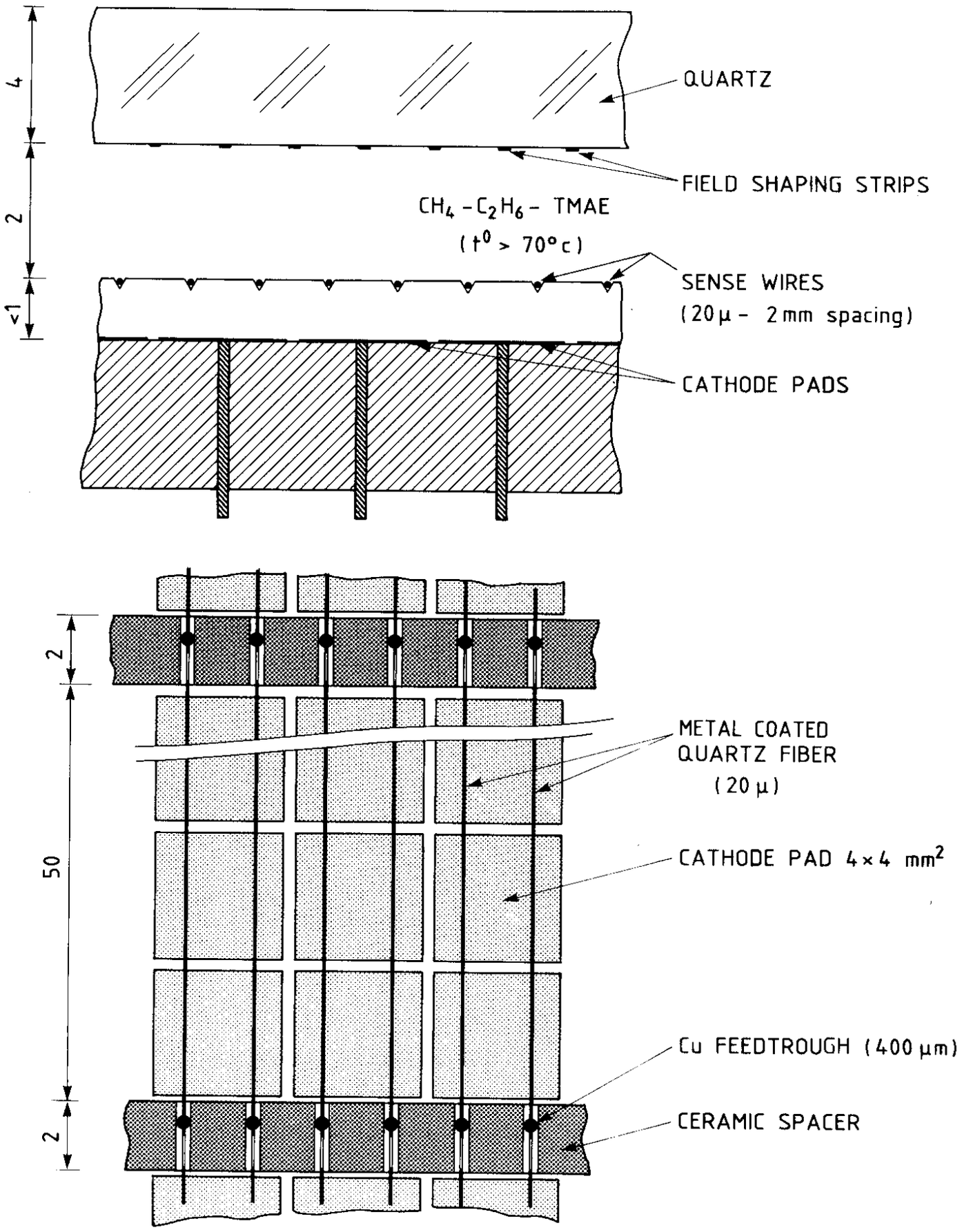
4
2
<1
QUARTZ
FIELD SHAPING STRIPS
$CH_4 - C_2H_6$ - TMAE
($t^0 > 70°C$)
SENSE WIRES
(20 µ - 2 mm spacing)
CATHODE PADS
2
50
2
METAL COATED
QUARTZ FIBER
(20 µ)
CATHODE PAD 4 × 4 mm²
Cu FEEDTROUGH (400 µm)
CERAMIC SPACER

Fig. 25